

AD-A163 465

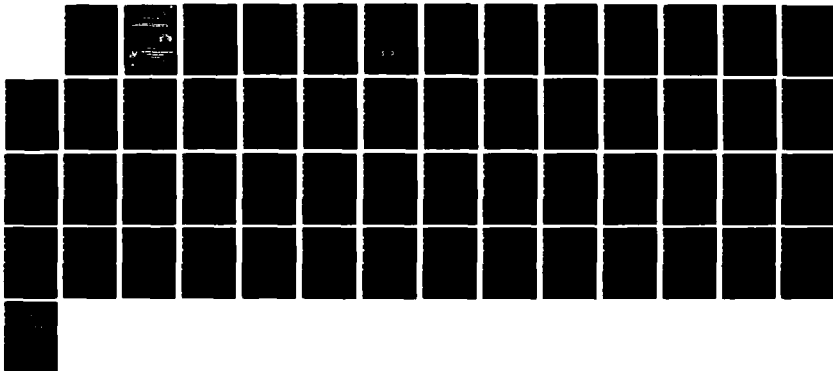
CARS (COHERENT ANTI-STOKES RAMAN SCATTERING)  
SPECTROSCOPY OF THE REACTION (U) ARMY ARMAMENT  
RESEARCH AND DEVELOPMENT CENTER DOVER NJ ARMAHE  
L E HARRIS JAN 86 ARAD-TR-85807

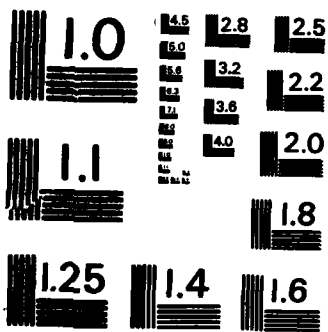
1/1

UNCLASSIFIED

F/G 19/1

NL





MICROCOPY RESOLUTION TEST CHART  
NATIONAL BUREAU OF STANDARDS-1963-A

AD-A163 465

ALL INFORMATION CONTAINED HEREIN IS UNCLASSIFIED

DATE 11-11-88 BY 60322 UCBAW

86 1 22 001

The views, opinions, and/or findings contained in this report are those of the author(s) and should not be construed as an official Department of the Army position, policy, or decision, unless so designated by other documentation.

The citation in this report of the names of commercial firms or commercially available products or services does not constitute official endorsement by or approval of the U.S. Government.

Destroy this report when no longer needed. Do not return to the originator.

UNCLASSIFIED

SECURITY CLASSIFICATION OF THIS PAGE (When Data Entered)

REPORT DOCUMENTATION PAGE		READ INSTRUCTIONS BEFORE COMPLETING FORM
1. REPORT NUMBER Technical Report ARAED-TR-85007	2. GOVT ACCESSION NO. A163465	3. RECIPIENT'S CATALOG NUMBER
4. TITLE (and Subtitle) CARS SPECTROSCOPY OF THE REACTION ZONE OF METHANE-NITROUS OXIDE AND RDX PROPELLANT FLAMES		5. TYPE OF REPORT & PERIOD COVERED October 1984 - September 1985
		6. PERFORMING ORG. REPORT NUMBER
7. AUTHOR(s) L. E. Harris	8. CONTRACT OR GRANT NUMBER(s)	
9. PERFORMING ORGANIZATION NAME AND ADDRESS ARDC, AED Energetics and Warheads Div (SMCAR-AEP-R) Dover, NJ 07801-5001		10. PROGRAM ELEMENT, PROJECT, TASK AREA & WORK UNIT NUMBERS
11. CONTROLLING OFFICE NAME AND ADDRESS ARDC, IMD STINFO Div (SMCAR-MSI) Dover, NJ 07801-5001		12. REPORT DATE January 1986
		13. NUMBER OF PAGES 54
14. MONITORING AGENCY NAME & ADDRESS (if different from Controlling Office)		15. SECURITY CLASS. (of this report)  Unclassified
		15a. DECLASSIFICATION/DOWNGRADING SCHEDULE
16. DISTRIBUTION STATEMENT (of this Report)  Approved for public release; distribution unlimited.		
17. DISTRIBUTION STATEMENT (of the abstract entered in Block 20, if different from Report)		
18. SUPPLEMENTARY NOTES This was presented at the Tenth International Colloquium on Dynamics of Explosives and Reactive Systems, Berkeley, CA, August 1985. This project was initiated in October 1984 by the Large Caliber Weapons Systems Laboratory, Applied Science Division, ARDC.		
19. KEY WORDS (Continue on reverse side if necessary and identify by block number) CARS Nitramine propellant RDX composite combustion Propellant decomposition		
20. ABSTRACT (Continue on reverse side if necessary and identify by block number) CARS spectra were obtained for a $\phi = 3.2$ CH <sub>4</sub> /N <sub>2</sub> O model and nitramine propellant flames throughout the reaction and post-flame zones in order to assess kinetic mechanisms occurring in these flames. Spectra were obtained in the regions of 4200 - 3900, 2400 - 2050, and 1900 - 1200 cm <sup>-1</sup> . The reaction zone of the rich CH <sub>4</sub> /N <sub>2</sub> O flame was studied primarily to provide a stationary flame analog to the transient propellant flame. In the CH <sub>4</sub> /N <sub>2</sub> O flame, the decay of the initial products was observed through the Q-branch of the $\nu_1$ and $\nu_3$ modes (cont)		

DD FORM 1 JAN 73 1473 EDITION OF 1 NOV 65 IS OBSOLETE

UNCLASSIFIED

SECURITY CLASSIFICATION OF THIS PAGE (When Data Entered)

## 20. ABSTRACT (cont)

of N<sub>2</sub>O and the Q, O, and S branches of the  $\nu_2$  and  $2\nu_2$  modes of CH<sub>4</sub>. The formation of the products N<sub>2</sub>, H<sub>2</sub> [Q( $\nu'' = 0$  and  $\nu'' = 1$ ) and S(5) - S(9)], CO, and CO<sub>2</sub> ( $\nu_1$ ) were also observed. Temperatures were obtained from both the H<sub>2</sub> and N<sub>2</sub> Q-branches. In the nitramine propellant flame, the upper bound of the gas-surface interface temperature was measured as  $900 \text{ K} \pm 100 \text{ K}$  from the H<sub>2</sub> Q-branch. Near the surface of the propellant, reactant RDX ( $1599 \text{ cm}^{-1}$  tentatively assigned as asymmetric NO<sub>2</sub> stretch) and transients HCN ( $\nu_1$ ) and NO are observed at moderate concentration (>1%). The final product N<sub>2</sub> is observed at low concentration (~1%), H<sub>2</sub> (Q and S branches) and CO are observed at higher concentration (>10%). RDX and HCN decay within 2 mm of the propellant surface while NO remains constant until 4 mm where it decays with a concomitant rise in N<sub>2</sub> concentration and temperature. H<sub>2</sub> and CO also increase in temperature and concentration.

The reaction zone of nitramine propellant is seen to consist of two characteristic areas: (1) an inner flame area near the solid gas-interface which is at a temperature of  $900 \pm 100 \text{ K}$  and is characterized by the gas-phase reactions of RDX and HCN that provide the heat that determines the burning rate, and (2) an outer flame area farther upstream where NO is converted to N<sub>2</sub> to generate the luminous flame.

CONTENTS

	Page
Introduction	1
Experimental	3
Results	5
Theory	5
CH <sub>4</sub> /N <sub>2</sub> O Flame	6
Nitramine Propellant Flame	8
Discussion	10
Conclusions	13
References	15
Distribution List	39

**S** DTIC  
ELECTE **D**  
JAN 22 1988  
B

Accession For	
NTIS GRA&I	<input checked="" type="checkbox"/>
DTIC TAB	<input type="checkbox"/>
Unannounced	<input type="checkbox"/>
Justification	
By _____	
Distribution/	
Availability Codes	
Dist	Avail and/or Special
A-1	



## TABLES

	Page
1 Laser dyes	19
2 Summary of species identified in a $\phi = 3.2$ $\text{CH}_4/\text{N}_2\text{O}$ flame	20
3 Summary of species identified in nitramine propellant flame	21

## FIGURES

1 CARS spectra of $\text{N}_2\text{O}$ , $\text{CO}$ , $\text{N}_2$ , and $\text{H}_2$ S(9) from a $\phi = 3.2$ $\text{CH}_4/\text{N}_2\text{O}$ flame	23
2a CARS spectra of $\text{CH}_4$ ( $\nu_2$ ) and $\text{H}_2$ S(7) and S(6) from a $\phi = 3.2$ $\text{CH}_4/\text{N}_2\text{O}$ flame	24
2b CARS spectra of $\text{CH}_4$ ( $\nu_2$ ) and $\text{H}_2$ S(5) and S(6) from a $\phi = 3.2$ $\text{CH}_4/\text{N}_2\text{O}$ flame	25
3 CARS spectra of $\text{N}_2\text{O}$ and $\text{H}_2$ S(5) from a $\phi = 3.2$ $\text{CH}_4/\text{N}_2\text{O}$ flame	26
4 CARS spectra of $\text{CH}_4$ ( $2\nu_2$ ) from a $\phi = 3.2$ $\text{CH}_4/\text{N}_2\text{O}$ flame	27
5 CARS spectra of $\text{H}_2$ Q-branch ( $\nu'' = 0$ ) in a $\phi = 3.2$ $\text{CH}_4/\text{N}_2\text{O}$ flame	28
6 CARS spectra of $\text{H}_2$ Q-branch ( $\nu'' = 0$ and $\nu'' = 1$ ) in a $\phi = 1.8$ $\text{CH}_4/\text{N}_2\text{O}$ flame	29
7 Time-averaged CARS spectra of $\text{N}_2$ at various distances above the surface of a nitramine propellant flame	30
8 Time-resolved CARS spectra of $\text{N}_2$ at various times after ignition at 2-mm above the surface of a nitramine propellant	31
9 Time-averaged CARS spectra of $\text{HCN}$ , $\text{CO}$ , $\text{N}_2$ , and $\text{H}_2$ S(9) above the surface of a nitramine propellant flame	32
10 Time-averaged CARS spectra of $\text{NO}$ and $\text{H}_2$ S(7) above the surface of a nitramine propellant	33
11 Time-averaged CARS spectra of $\text{RDX}$ (tentative), $\text{H}_2$ S(5), and $\text{CO}_2$ above the surface of a nitramine propellant	34
12 Time-resolved (single shot) CARS spectra of the $\text{H}_2$ Q branch taken at nominal 6-second intervals after ignition, and shown sequentially from bottom to top	35

- 13 Time-resolved (10-shot averaged) CARS spectra of the H<sub>2</sub> Q branch taken at nominal 6-second intervals after ignition and shown sequentially from bottom to top 36
- 14 Time-resolved (3-shot averaged) CARS spectra of the H<sub>2</sub> Q branch taken at nominal 6-second intervals after ignition and shown sequentially from bottom to top 37

## INTRODUCTION

Obtaining direct experimental information on the dynamics of the deflagration and detonation of energetic materials has been difficult with the use of conventional optical techniques. The advent of nonlinear optical techniques such as Coherent Anti-Stokes Raman Scattering (CARS) provides an opportunity to extend the information obtainable on energetic systems. Propellant flames are often transient, particle-laden, incandescent, and, under some conditions, turbulent. However, single-shot CARS spectra were obtained from the post-flame region of double-base propellant flames (Harris and McIlwain, refs 1 and 2). This demonstration of the direct applicability of CARS to obtaining temperature and concentration from propellant flames led to further investigations in the reaction zone and post-flame region of  $\text{CH}_4/\text{N}_2\text{O}$  model propellant flames (Harris, refs 3 and 4 and Aron et al., ref 5). These studies were then extended to the reaction zone of nitramine propellant flames through measurements at the surface and at 6-mm above the propellant surface (Aron and Harris, ref 6 and Harris, ref 7). In these studies both the spectral and spatial ranges are extended for the reaction zone of  $\text{CH}_4/\text{N}_2\text{O}$  and nitramine propellant flames. Rich  $\text{CH}_4/\text{N}_2\text{O}$  flames are used as stationary model flames of the transient propellant flames.

The combustion of nitramine propellants was reviewed recently by Boggs (ref 8) and Schroeder (ref 9). Nitramine propellants contain a substantial percentage of nitramines (~76%) along with a small percentage of energetic binder (~4% nitrocellulose) and/or organic-ester binders. Current models of nitramine propellant combustion are essentially models of HMX (cyclotetramethylene tetranitramine) and RDX (hexahydro-1,3,5-trinitro-s-triazine deflagration). The burning rate expression for nitramine propellants (Ben-Reuven and Caveny, ref 10)

$$r = ap^{1/2} (1 + p/b)^{1/2}$$

is such that at low pressure

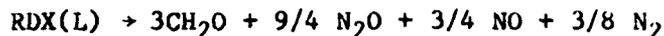
$$p \ll b, r \sim p^{1/2}$$

whereas at high pressure

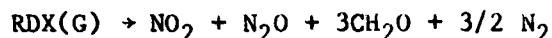
$$p \gg b, r \sim p^1$$

Much of the modeling of nitramine propellant has been to explain this complex burning rate behavior. Ben-Reuven and Summerfield (ref 11) have reviewed nitramine propellant modeling and derived improvements to the comprehensive model of nitramine deflagration (Ben-Reuven and Caveny, ref 10). The Ben-Reuven and Caveny model consists of the following mechanism:

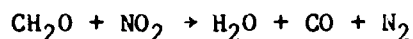
First, partial decomposition of RDX in the liquid phase



Next, gas phase decomposition of RDX in the near field (close to the propellant surface)



Finally, oxidation of formaldehyde by  $\text{NO}_2$



in the far field (relatively far from the propellant surface).

Thermocouple measurements of temperature profiles in nitramine/polyurethane composite propellants were made by Kubota (ref 12). He obtained surface temperatures between 690 K to 730 K in the pressure range between 10 to 30 atm. Kubota found from flame quenching studies that both RDX and the polymeric binder melt at the surface to produce an homogeneous liquid layer that produces an homogeneous flame. The flame was found to consist of dark and luminous flame zones with the luminous zone approaching the propellant surface with increasing pressure. The measured dark zone thickness at 20 atm for a 75% RDX formulation was 2-mm. The dark zone thickness was observed to vary inversely with the square of increasing pressure. At 1,000 psi, the dark zone would be compressed to 200  $\mu\text{m}$ , spatially limiting accessibility for optical diagnostics. The luminous flame, however, would still be accessible to optical diagnostics. According to Kubota, the dark zone reaction can be attributed to NO reduction to  $\text{N}_2$  to produce the luminous flame. The burning rate was found to be controlled not by the luminous flame but rather by exothermic reactions of RDX at the propellant surface.

Ben-Reuven and Summerfield (ref 11) have added to the Ben-Reuven and Caveny (ref 10) model, a nonequilibrium evaporation law at the melt-gas interface, an improved melt phase model including a decomposition-gas bubble, and an improved model for far-field processes including several simultaneous secondary reactions.

Schroeder (ref 9) has reviewed nitramine decomposition chemistry. At low temperature (500 to 600 K), the gas phase reaction mechanism by which RDX initially decomposes is postulated as



This is thought to occur through HONO elimination and/or cyclic decomposition via the intermediate N-nitroformimine,  $\text{CH}_2\text{NNO}_2$ . Crossover to a high temperature reaction mechanism in the gas phase is thought to occur above about 600 K.

This mechanism is thought to occur via breakage of an initial NN bond followed by fragmentation to  $\text{CH}_2\text{NNO}_2$  which decomposes to HCN and  $\text{NO}_2$ , leading to the overall initial reaction.



The liquid phase reaction is also thought to occur by a mechanism similar to the high temperature gas phase reaction mechanism.

Price et al. (ref 13) modified the Beckstead-Derr-Price (BDP) framework for HMX decomposition to incorporate both the high (endothermic) and low (exothermic) temperature nitramine decomposition mechanisms in the solid and exothermic and endothermic second-order reactions in the gas phase. Cohen et al. (ref 14) explicitly included reactions of HCN and NO in the BDP model.

Miller and Coffee (refs 15 and 16) gave detailed comparisons of the various methods used to model propellant combustion. Their assessment was that the methods place too much emphasis on matching experimental burning rate data which are relatively insensitive to mechanistic details. They conclude that mechanisms used in propellant modeling should be independently validated. Propellant surface temperature,  $T_s$ , enters many of these models as a parameter used to match experimental burning rates. Independent measurement of  $T_s$  will allow validation and further development of these models.

CARS spectroscopy, which was reviewed by Druet and Taran (ref 17) and Ecbreth and Schreiber (ref 18), provides an ideal tool for the further elucidation of nitramine propellant kinetic mechanisms. CARS has the necessary spatial (100  $\mu\text{m}$ ), temporal (10 ns single shot), and spectral resolution to provide the detailed temperature, concentration, and rovibrational state distribution profiles necessary to successfully model propellant flames from independently measured elementary kinetic reactions (Gardner, ref 19).

## EXPERIMENTAL

CARS spectra are generated with folded BOXCARS to achieve phase matching. The output of a Quanta-Ray DCR-2A Nd/YAG laser at 1.06  $\mu\text{m}$  (700 mj) is doubled to generate the pump beam at 5320A (250 mj) with a bandwidth of near 1  $\text{cm}^{-1}$ . The pump beam is separated from the primary beam with prisms. The pump beam is split to generate  $\omega_{1s}$  and  $\omega_{1p}$ .  $\omega_{1s}$  is used to pump a dye laser to generate the Stokes beam,  $\omega_2$ . The dye laser consists of a flowing dye cell in a planar Fabry-Perot oscillator cavity pumped slightly off axis by 20% of  $\omega_{1s}$  with the output amplified by an additional flowing dye cell pumped by the remainder of  $\omega_{1s}$ . The dye laser is operated broadband with the laser dyes given in table 1. To achieve BOXCARS geometry,  $\omega_{1p}$  is reflected onto the front surface of a dichroic mounted at a 45 degree angle. The dichroic reflects 50% of  $\omega_{1p}$  from half of its front surface and 100% of the remainder of  $\omega_{1p}$  from its back surface while transmitting  $\omega_2$  which is introduced from the rear below  $\omega_{1p}$ .  $\omega_{1p}$  is split into two beams,  $\omega_1$

and  $\omega_1'$ , such that at the focusing lens (200 mm focal length)  $\omega_1$ ,  $\omega_1'$ , and  $\omega_2$  are parallel and situated on a circle of 12.5 mm diameter with  $\omega_1$  and  $\omega_1'$  on the central horizontal plane of the lens with  $\omega_2$  in the central vertical plane. Telescopes are inserted in the  $\omega_{1p}$  and  $\omega_2$  beams to allow the focal spots to be equalized and intersecting. This was achieved with 0.85 and 2 X Galilean telescopes in  $\omega_{1p}$  and  $\omega_2$ , respectively. A 5-mm-diameter iris centered on  $\omega_{1p}$  prior to splitting further restricts intersection to the central portion of  $\omega_{1p}$ . To optimize phase matching, a 12.5-mm-thick optical flat--rotatable about its horizontal axis--is inserted into  $\omega_2$  before the focusing lens. After passage through the sample, the beams are recollimated with a 200-mm focal length lens, after which  $\omega_3$  is located below the plane of  $\omega_1$  and  $\omega_1'$ .  $\omega_1$ ,  $\omega_1'$ , and  $\omega_2$  are terminated with a neutral density filter.  $\omega_3$  is then focused with a 100-mm focal length lens onto the slits of a 1/3-m monochromator equipped with a 2,400 line/mm holographic grating and 100  $\mu$ m slits. The signal is detected by a PAR SIT detector and processed by a PAR OMA2 system. The full width at half-height (FWHH) of calibration lines near the center of the SIT detector is near 3.0  $\text{cm}^{-1}$ , giving approximately 1  $\text{cm}^{-1}$  per channel over the spectral range investigated.

Stationary flame measurements were made on a premixed  $\text{CH}_4/\text{N}_2\text{O}$  flame maintained on a circular burner with a 2.0-cm-diameter head. The burner surface was constructed of a matrix of steel syringe needles of 0.09-cm outer diameter, so that a flat flame would be achievable under suitable flow conditions. Matheson technical grade methane and chemically pure nitrous oxide were separately flowed through 603 Matheson rotameters prior to premixing. The flow through the burner was adjusted to 13 cm/sec to maintain a 3.2 equivalence ratio ( $\phi$ ) flame where  $\phi$  is defined here as the fuel/oxidant ratio divided by the stoichiometric fuel/oxidant ratio. At this flow, there is a dark zone extending about 5-mm above the burner surface followed by a dark yellow reaction zone extending to about 13-mm above the burner. A bright yellow post flame region surrounded by a light blue afterburning diffusion flame was situated above the reaction zone. To obtain CARS spectra in the reaction zone, the center of the burner surface was displaced vertically with a translation stage from the focus of  $\omega_1$ ,  $\omega_1'$ , and  $\omega_2$  to 2 cm below the focus. Spectra were obtained at intervals of 0.5 mm (0.25 mm in the vicinity of the reaction zone). The flame exhibited macroscopic structure since the position of the reaction zone fluctuated with respect to the burner surface. Spectral scans through the reaction zone were obtained in periods of stability between these large scale fluctuations. Spectra obtained at the same positions relative to the position of initial attainment of full flame temperature were reproducible within the precision of the flowmeters.

The nitramine propellant grains were 14 x 14 mm cylinders of mass 3.2 g. The propellant grains were burned in air with spectra taken along the centerline above the burning propellant surface during the approximately 1-minute burn time. The propellant flame can be characterized as consisting of an inner dark zone approximately 4 mm thick, a bright yellow post flame region, and an outer blue diffusion flame. The calculated gas velocity from the burning cylinder is approximately 50 cm/sec.

## RESULTS

### Theory

The observed CARS spectrum is proportional to the square of the modulus of the third-order susceptibility,  $\chi^{(3)}$ , which is the sum of a resonant term  $\chi_r$  related to a nuclear displacement and  $\chi_{nr}$  related to electronic displacement:

$$\chi^{(3)} = \chi_r + \chi_{nr} \quad (1)$$

The resonant term can be considered as a sum of Lorentzian line shapes of each Q(J), O(J), or S(J) transition (Tolles et al., ref 20 and Hall, ref 21).

$$\chi_r = \sum_j \frac{k_j \Gamma_j}{2\Delta\omega_j - i \Gamma_j} \quad (2)$$

where

$$k_j = (N/m\omega_0) |M_j|^2 (\Delta j) \Gamma_j^{-1} \quad (3)$$

where  $M_j$ ,  $\Delta j$ ,  $\Gamma_j$  are the polarizability matrix element, normalized population difference, and line width, respectively;  $\Delta\omega_j$  is  $\omega_1 - \omega_2 - \omega_j$ ;  $m$  is the reduced mass; and  $\omega_0$  is the resonant Raman frequency.  $M_j = \alpha^2 (\nu + 1)^j$  and  $7/45 b_j \pm 2^j \gamma^2 (\nu + 1)$  for Q and O, S branches, respectively. Where  $\alpha$ ,  $\gamma$ , and  $b_j$  are the derivatives of the mean isotropic and anisotropic molecular polarizability, and  $b_j$  are the Placzek-Teller coefficients,  $\nu$  is the vibrational quantum number and  $(\nu + 1)$  is contributed by the vibrational matrix element. The observed spectrum is convoluted over the laser linewidths and instrumental slit function.

$\chi_r$  is the sum of real and imaginary components  $\chi'$  and  $\chi''$ , respectively, such that

$$|\chi^{(3)}|^2 = \chi'^2 + 2 \chi' \chi'' + \chi''^2 + \chi_{nr}^2 \quad (4)$$

$\chi'$  and  $\chi''$  display dispersive and resonant behavior, respectively. Normalizing equation 4 with respect to the observed  $\chi_{nr}^2$  at the resonance gives

$$\left( \frac{|\chi^{(3)}|^2}{\chi_{nr}^2} \right)_0 = \left| \frac{\chi i(i k_j)}{\bar{\chi}_{nr}} + 1 \right|^2 \quad (5)$$

where  $\bar{\chi}$  and  $\bar{k}$  are defined as  $\chi/N$  and  $k/N$ , respectively and  $X_i = N/N_T$  with  $N$  and  $N_T$ , the number density of the resonant species and the total number density, respectively.

Summing of equation 5 over the populated levels gives:

$$\Sigma I_{\text{corr}}^2 = \Sigma (1/g_j)^2 (|\chi^{(3)}|^2 / \bar{\chi}_{\text{nr}}^2)_0 = \left[ X_i \frac{\Sigma \bar{k}_j}{\bar{\chi}_{\text{nr}}} + 1 \right]^2 \quad (6)$$

where  $\bar{k}_j = \frac{|\bar{M}|^2}{m \omega_0 \Gamma_j}$  since  $\Sigma \Delta_j / g_j = 1$

$g_j = (\nu + 1)$  for Q branches without rotational structure and  $(2J + 1) n_j (\nu + 1)$  for O and S branches where  $n_j$  is the nuclear spin degeneracy.  $\Gamma_j$  is taken as the experimentally observed spectral line width,  $\Gamma_{\text{exp}}$ , since the observed CARS intensity,  $|\chi^{(3)}|^2$ , is convoluted by the instrument function. If the peak height is measured from the maximum to the minimum of the resonant peak modulation of the nonresonant background spectra, only the imaginary term is measured (Tolles et al., ref 20) so that

$$X_i = \frac{(\Sigma I_{\text{corr}})^{1/2}}{(\Gamma_{\text{exp}} m \omega_0) \bar{\chi}_{\text{nr}} / \bar{M}^2} \quad (7)$$

with  $\bar{M} = \alpha^2$  and  $7/45 \gamma^2$  for Q branches (where anisotropic contributions are neglected) and O,S branches, respectively. Equation 7 forms the basis for a qualitative interpretation of the spectra. Concentration and temperature are separable such that concentration is related to the sum of  $I_{\text{corr}}$  while temperature is related to the ratio of  $I_{\text{corr}}$  of populated levels. Equation 7 was used to obtain relative concentrations through the reaction zone discussed below. In addition, for  $N_2$  and  $H_2$  the spectra were synthesized using the method of Hall (ref 21) and fitted to the experimental spectra using a least-square procedure to obtain temperature and concentration.

### CH<sub>4</sub>/N<sub>2</sub>O Flames

Thermochemical calculations (Gordon and McBride, ref 22) were performed for  $\phi = 3.2$  CH<sub>4</sub>/N<sub>2</sub>O. The calculated flame temperature was 1745 K with 23% CO, 1% CO<sub>2</sub>, 42% H<sub>2</sub>, 5% H<sub>2</sub>O, and 29% N<sub>2</sub>. CARS spectra were obtained in the regions 4200 to 3900, 2400 to 2050, and 1900 to 1200 cm<sup>-1</sup> as a function of distance above the center of the surface of the burner. The spectra are given in figures 1 through 7 and summarized in table 2.

Reaction occurs over a region extending from 2 mm to 12 mm with the steepest concentration gradients occurring between 6 mm to 10 mm. The flame may be roughly characterized as consisting of a dark or preheating zone extending from the surface to 6 mm, a reaction zone extending from 6 mm to 10 mm and a post flame region above 10 mm. The spectra shown in figures 1 through 6 show one representative spectra from each of these regions.

The spectra shown in figure 1 show the decay of reactant  $N_2O$  and the increase of the products  $N_2$ ,  $CO$ , and  $H_2$ . The  $N_2O$   $\nu_3$  at  $2222\text{ cm}^{-1}$  and associated hot bands already have been observed and assigned from spectra occurring in the reaction zone of lean  $CH_4/N_2O$  flames (Harris, refs 23 and 24). The  $N_2$  and  $CO$  vibrational and the  $H_2$  pure rotational S(7) [The notation used is S( $\nu''$ )] spectra have previously been discussed for spectra arising from the post flame region of rich  $CH_4/N_2O$  flames (Aron et al., ref 5). The simultaneous observation of the decay of  $N_2O$  and the increase of the three principal products provides an opportunity to obtain concentration gradients to test kinetic mechanisms.

Spectra shown in figure 2 show the decay of the other reactant together with the increase of product  $H_2$  S(7) and S(6) pure rotational lines. The  $CH_4$  structure shown in figure 2 is assigned to  $\nu_2$  transitions. The prominent features of the methane transitions are observed\* at the following frequencies ( $\text{cm}^{-1}$ ): 1531, 1562, 1583, 1606, 1628, 1653, 1676, 1722, 1745, 1769, and 1792. This is in agreement with previously observed (Champion and Berger, ref 25) and calculated (Gray and Robiette, ref 26) Raman lines at the following frequencies ( $\text{cm}^{-1}$ ): 1534 (Q), 1566 [S(0)], 1587 [S(1)], 1610 [S(2)], 1632 [S(3)], 1654 [S(4)], 1677 [S(5)], 1724 [S(7)], 1746 [S(9)], and 1770 [S(10)], assuming a separation of 4B for a ground state B value of  $5.24\text{ cm}^{-1}$  (Gray and Robiette, ref 26).

$N_2O$  and  $H_2$  S(5) spectra are shown in figure 3. The  $N_2O$  CARS at 1284, 1290, and  $1295\text{ cm}^{-1}$  transitions (not previously reported) are assigned to the  $\nu_1$  and  $\nu_1 + \nu_2 - \nu_2$  and  $\nu_1 + 2\nu_2 - 2\nu_2$  in agreement with transitions observed<sup>1</sup> in the Raman at  $1285\text{ cm}^{-1}$  and calculated at  $1289.7\text{ cm}^{-1}$  (Herzberg, ref 27). The  $\nu_1$  transition has a larger Raman cross section than the  $\nu_3$  together with hot bands populated at low temperature, providing an attractive option for quantitative temperature and concentration profiles in the reaction zone.

The decay of the  $CH_4$  2  $\nu_2$  band is shown in figure 4. The observed bands ( $\text{cm}^{-1}$ ) are 3101 (Q), 3129 [S(0)], 3149 [S(1)], 3168 [S(2)], 3182 [S(3)], 3205 [S(4)], 3223 [S(5)], 3235 [S(6)], and 3258 [S(7)]. These are in agreement with assignments given by Hunt et al. (ref 28). Hydrogen Q band structure as it increases through the reaction zone is given in figure 5. Hydrogen is seen at a concentration less than 1% at 4 mm. The line positions as shown for  $\nu'' = 0$  in figure 5 and  $\nu'' = 0\text{ J} < 11$  and  $\nu'' = 1\text{ J} < 9$  in figure 6 and the S bands  $J = 5$  to 9 have been shown to be in excellent agreement with the results of constants derived from ab initio calculations (Fendell et al., ref 29) and constants (Dabrowski, et al., ref 30) derived from the  $B^3\Sigma^+ \leftarrow X^1\Sigma^+$  and  $C^1\Pi \leftarrow X^1\Sigma^+$  band of  $H_2$  (Haw et al., ref 31).

Temperature was calculated from the  $\nu'' = 0$  Q branch throughout the reaction zone. From 4 to 8 mm, there is a gradual increase in temperature from 500 K to 900 K and the distribution appears Boltzmann. Above 8 mm, there is an apparent bimodal distribution in which approximately half of the observed spectra have Boltzmann distributions consistent with the random experimental error while the other spectra show much larger deviations from the Boltzmann distribution (greater than  $2\sigma$ ) than the random experimental error. In these non-Boltzmann distributions, the odd levels are preferentially populated over the even levels with

\* Some lines were observed with the use of other dyes.

the higher J value of both even and odd levels showing excess population. At present, it is not certain whether these apparently non-Boltzmann distributions reflect the actual hydrogen rotational distributions, instrument errors, or flame instability for hydrogen above the reaction zone. Flame stability lessens with distance above the burner. The outer blue diffusion flame is noticeably floppy. Further work is being done in more stable rich  $\text{CH}_4/\text{N}_2\text{O}$  flames to clarify the interpretation of the hydrogen Q branch spectra. The  $\text{H}_2$  spectra that have Boltzmann distributions give results consistent with temperatures obtained from  $\text{N}_2$  CARS spectra and thermochemical calculations.

$\text{N}_2$  CARS spectra in the reaction zone are difficult to interpret because of the unknown non-resonant susceptibility. However, in the post flame region least-squares-fits to the  $\text{N}_2$  spectra give a temperature of  $1890 \pm 100$  K and concentration of  $0.26 \pm 0.05$  m (mole fraction) which are close--although slightly high for temperature--to the results of the thermochemical calculations.

### Nitramine Propellant Flames

Thermochemical calculations (Gordon and McBride, ref 22) were performed for the nitramine propellant with the result that the adiabatic, constant pressure, flame temperature was calculated as 2076 K with the equilibrium final products calculated as 38%  $\text{CO}$ , 27%  $\text{H}_2$ , 22%  $\text{N}_2$ , 10%  $\text{H}_2\text{O}$ , and 3%  $\text{CO}_2$ . CARS spectra were obtained in the regions 4200 to 3900, 2400 to 2050, and 1900 to 1200  $\text{cm}^{-1}$  both as a function of distance above the center of the propellant surface and time at a given initial distance. The spectra are given in figures 7 through 14 and summarized in table 3. The 14 mm high grain burns in approximately 60 sec for an average burning velocity of 0.2 mm/s. The average flow calculated is 50 cm/s assuming that the cylindrical geometry is retained throughout the burn (a residual residue retaining approximately the original cylindrical geometry is retained throughout much of the burn). In the middle of the burn, the propellant flame consists of: (1) a dark region extending 4 mm above the propellant surface; (2) a conical dark yellow post flame region above the dark zone and extending to 3 cm above the propellant surface; and (3) a conical blue after-burning diffusion flame of  $\text{CO}$ ,  $\text{H}_2$ , and air extending to 8 cm above the propellant surface. The initial region of steepest formation of  $\text{N}_2$  occurs from 3 to 6 mm above the propellant surface. The flame was smaller during ignition and extinguishment (the initial and final 10 sec, approximately).

Average spectra (100 scans, 10 sec) were taken as a function of distance from the propellant surface to 6 mm above the surface at intervals of 1 mm. Each spectrum was taken nominally 10 sec after ignition. In addition, time sequences of 10 scans (1 sec) spectra were taken approximately every 6 sec from ignition to extinguishment. For  $\text{H}_2$ , the intensity of the signal permitted the acquisition of single-shot spectra.

The  $\text{N}_2$  spectrum as a function of distance above the propellant surface is shown in figure 7.  $\text{N}_2$  appears at low concentration (<1%) at the propellant surface and gradually increases to final concentration near 6 mm. Time-resolved  $\text{N}_2$  spectra at 2 mm above the propellant surface are shown in figure 8.  $\text{N}_2$  is seen initially at low concentration and takes more than half the burn time to approach equilibrium concentration.

The CO region is shown in figure 9. CO is seen at higher concentration than  $N_2$  at the surface with an increase in temperature most evident with increasing distance above the surface. A peak at the frequency of HCN at  $2086\text{ cm}^{-1}$  was moderately strong at the surface and 1 mm but had decayed by 2 mm to reveal the CO hot band at  $2080\text{ cm}^{-1}$ . In addition,  $N_2$  and  $H_2$  S(9) at  $2129\text{ cm}^{-1}$  are seen to be in approximately constant ratio to CO above 2 mm. In time-resolved spectra of this region (not shown), near the end of the burn (55 sec after ignition), CO and  $H_2$  are no longer present and only the  $N_2$  resonance is seen.

NO and  $H_2$  S(7) spectra are shown in figure 10 as a function of distance above the propellant surface. NO is seen as a modulation of the non-resonant background. However, since NO has a Raman cross section only half that of  $N_2$ , the concentration of NO may be greater than 1% at the surface. In time-resolved spectra NO is seen to persist until the steep increase in  $N_2$  which occurs at about 4 mm above the propellant surface. The  $H_2$  S(7) band is seen to undergo a continuous increase with distance above the propellant surface up to 6 mm.

Prominent spectra at  $1599\text{ cm}^{-1}$  tentatively associated with the RDX  $NO_2$  asymmetric stretch transition reported at  $1596\text{ cm}^{-1}$  in the Raman spectrum of RDX powder (Iqbal et al., ref 32),  $H_2$  S(5) at  $1446\text{ cm}^{-1}$ , and  $CO_2$  at  $1387\text{ cm}^{-1}$  are shown in figure 11. The  $1599\text{ cm}^{-1}$  transition is present at the surface and at 1.0 mm but absent at 3.0 mm. The  $H_2$  S(5) transition is seen to increase relative to  $CO_2$ . This is consistent with the final equilibrium concentrations of these species. At 1 mm, the moderate intensity feature between  $H_2$  and  $CO_2$  near  $1408\text{ cm}^{-1}$  is seen to be complex and tentatively associable with  $CO_2$  and HCN bending modes (Harris, ref 7).

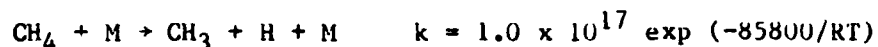
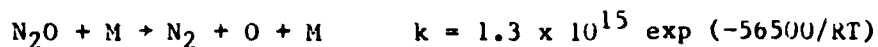
Time-resolved spectra of  $H_2$  Q branch at the propellant surface are given in figures 12 through 14. The  $H_2$  Q branch has a cross section twice as large as nitrogen, and hydrogen is present at high concentration throughout the propellant flame so that the hydrogen Q branch spectra are not perturbed appreciably by the non-resonant susceptibility. This simplified interpretation of the spectra to obtain temperature. As shown in figure 12, single shot spectra are obtained at good signal-to-noise and are in substantial agreement with 10-shot averaged spectra. The reduction of the signal-to-noise from bottom to top is a reflection of the increasing temperature as a function of distance above the propellant surface. Temperatures have been obtained from the  $H_2$  Q branch spectra. The average temperature of the spectra taken at the surface is  $1000\text{ K} \pm 200\text{ K}$ . The dispersion reflects not only the noise in the individual spectra but also the variation of the distance of the surface with respect to the CARS sampling volume since spectra are taken as close to the surface as possible. A propellant surface/gas interface temperature is more properly associated with the lower bound of the propellant surface temperature measured with good signal-to-noise rather than the average surface temperature. The spectra shown in figure 14 are three-shot averages and are near the lower bound of measured surface/gas interface temperatures. The lower two spectra were least-squares fit to a temperature of  $900 \pm 100\text{ K}$  which may then be associated with an upper bound of the surface/gas interface temperature. Time-resolved  $H_2$  Q branch CARS spectra taken at the surface during the duration of the propellant burn were used to obtain temperature. (The spectra used were Boltzmann within experimental accuracy. The non-Boltzmann distributions were not obtained with the frequency encountered in  $CH_4/N_2O$  flames.)

These spectra show an initial temperature of  $1000 \pm 200$  K with a gradual rise to  $1500 \pm 200$  K over the first 40 sec of the burn, then a sharp increase within a sec to  $2000 \pm 200$  K which is maintained for approximately 10 sec before a rapid rise to  $2600 \pm 200$  K at 55 sec of the burn. The initial gradual temperature rise to 1500 K may be associated with the dark zone while the steep temperature rise to 2000 K may be associated with the reaction zone of the adiabatic flame which culminates in flame temperature near the calculated adiabatic flame temperature of 2076 K. The subsequent steep temperature rise to 2600 K encountered at 55 sec into the burn is associated with the afterburning or diffusion flame of CO, H<sub>2</sub> with air. This is consistent with the absence of CO and H<sub>2</sub> at this time in time-resolved spectra discussed above. As in the CH<sub>4</sub>/N<sub>2</sub>O flame, flame stability decreases with distance above the surface of the propellant. Temperature and concentration were also obtained from N<sub>2</sub> spectra in the adiabatic post flame region as  $2010 \pm 115$  K and  $0.26 \pm 0.04$  which are in good agreement with the calculated values (2076 K and 0.22) and the temperature estimated from hydrogen spectra in this region ( $2000 \pm 200$  K). (N<sub>2</sub> spectra have not been analyzed in the dark and reaction zones because the composition of these regions is not yet sufficiently characterized to permit estimation of the nonresonant susceptibility.)

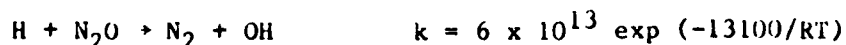
#### DISCUSSION

The reaction zone of the rich CH<sub>4</sub>/N<sub>2</sub>O flame was studied primarily to provide a stationary flame analog to the transient nitramine propellant flames. Since the rich CH<sub>4</sub>/N<sub>2</sub>O flame has similar atomic composition, adiabatic flame temperature, and final products as the propellant flame, it is to be expected that some features of the kinetic mechanisms will be similar in both systems. In the CH<sub>4</sub>/N<sub>2</sub>O flame, the decay of the initial products was observed through the Q branch of the  $\nu_1$  NN and  $\nu_3$  NO stretching modes of N<sub>2</sub>O and the Q, O, and S branches of the  $\nu_2$  and 2  $\nu_2$  modes of CH<sub>4</sub>. The formation of the products N<sub>2</sub>, H<sub>2</sub>, CO, and CO<sub>2</sub> was also observed.

No intermediate species were detected in the spectral range investigated. Initial decomposition of the reactants was observed to occur near 500 K. The first order rate constants for N<sub>2</sub>O (Balakhnine et al., ref 33) and CH<sub>4</sub> (Tabayaski and Bauer, ref 34)



preclude observable reaction at 500 K. However, secondary reactions for N<sub>2</sub>O given by Balakhnine



and Wagel et al (ref 35)

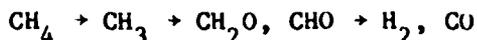


and  $\text{CH}_4$  given by Tabayaski and Bauer (ref 34)

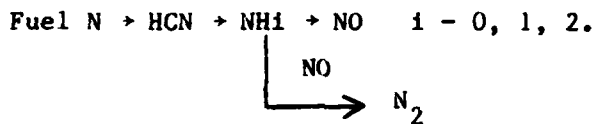


explain reactivity at 500 K.

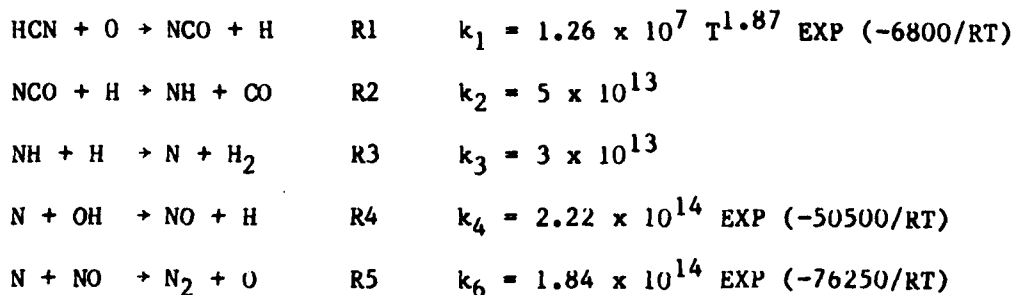
The conversion of methane to final product is thought to proceed by the following global mechanism (Westbrook and Dryer, ref 36)



The conversion of fuel-bound nitrogen is an area of active current research. Recently,  $\text{CH}_4/\text{O}_2/\text{AR}$  flames doped with HCN, NO, and  $\text{NH}_3$ ; and  $\text{H}_2/\text{O}_2/\text{AR}$  flames doped with HCN were studied by Zabielski (ref 37) and Miller et al. (ref 37), respectively. These and previous studies have shown that the conversion of fuel nitrogen to HCN is almost quantitative and independent of the chemical nature of the initial fuel nitrogen. Since conversion to HCN is not rate limiting, research has focused on conversion to NO and  $\text{N}_2$ . These processes are thought to occur by the global mechanism.



Good agreement between the theoretical and experimental temperatures and the concentration profiles in these studies has been obtained in terms of the following key reactions:



The reaction constant  $k_1$  is based on a measurement by Perry and Melius (ref 38);  $k_2$  is an estimate (Miller et al., ref 39); and  $k_3 - k_5$  are taken from a recent compilation (Miller et al., ref 40). These reactions, with the addition of the hydrocarbon combustion cycle given globally above, account qualitatively for the formation of the principal products  $\text{H}_2$ ,  $\text{N}_2$ , and CO in the rich  $\text{CH}_4/\text{N}_2\text{O}$  flame studied here. Further reduction of the data obtained from the  $\text{CH}_4/\text{N}_2\text{O}$  flame to quantitative temperature and concentration profiles will enable a quantitative test of these kinetic mechanisms. The results for  $\text{CH}_4/\text{N}_2\text{O}$ , as presented, provide a comparison for results obtained in nitramine propellants.

In nitramine propellant, the upper bound of the gas-surface interface temperature was measured at  $900 \pm 100$  K. To our knowledge, this is the first direct

measurement of the gas-surface interface temperature in the gas phase. The measured temperature was in good agreement with a propellant surface temperature of 700 K measured in the solid phase using thermocouples (Kubota, ref 12). Near the surface of the propellant reactant, RDX and transient species HCN and NO were observed at moderate concentration (>1%). The final product N<sub>2</sub> was observed at low concentration (~1%) while H<sub>2</sub> and CO were observed at higher concentration (>10%). A gradual temperature rise from the surface to 4 mm above the surface to 1500 K was observed, with a steep rise to 2000 K occurring near 4 mm. RDX and HCN were observed to decay within 2 mm of the surface with NO remaining constant to 4 mm. Near 4 mm, NO decayed rapidly with a concomitant increase in N<sub>2</sub> concentration and temperature to adiabatic flame temperature. H<sub>2</sub>, CO, and CO<sub>2</sub> increased in concentration throughout this region.

The physical structure of the flame is similar to that modeled by Ben-Reuven and Summerfield (ref 11) in terms of near field and far field reactions occurring in the dark zone. However, these results suggest that the chemistry in this model (Ben-Reuven and Caveny, ref 10) must be modified. The observation of HCN and lack of observation of N<sub>2</sub>O (<0.1%) is consistent with the high temperature (T>600 K) nitramine decomposition mechanism



NO<sub>2</sub>, although observable at low pressure in CARS, is not observable at atmospheric pressure--perhaps due to the adsorption by NO<sub>2</sub> in the region of the laser beams used in these experiments. Additional experiments are needed (laser fluorescence is a possibility) to determine the concentration of NO<sub>2</sub> in the reaction zone. NO<sub>2</sub> is presumably converted to NO by fast radical recombination reactions of NO<sub>2</sub> with H, N, and O (Baulch et al., ref 41).

Thus RDX decomposition in the flame differs from processes occurring in the CH<sub>4</sub>/N<sub>2</sub>O flame in that RDX decomposes directly into products that are thought to be the principal intermediates in the conversion of fuel-bound nitrogen to final products. This allows, in contrast to CH<sub>4</sub>/N<sub>2</sub>O processes, a substantial buildup of the intermediates HCN and NO near the propellant surface so that they are directly observable in CARS.

At these pressures, it is the decomposition processes of the species at the surface, RDX and HCN, which supply the heat that determines the burning rate of the nitramine propellant. NO conversion to N<sub>2</sub> which provides the heat for the luminous flame occurs too far upstream to affect the surface. HCN decomposition processes, which are given above, are initiated by R1. Since R1 depends on the oxygen concentration, the ignition of nitramine propellants depends critically on oxygen concentration. The steep rise in temperature to 2600 K indicates the presence of the afterburning reaction of hot CO and H<sub>2</sub> (which constitutes 65% of the products) with air. This reaction serves to shield the inner flame from the influence of atmospheric oxygen and serves as a flame holder for the inner flame.

## CONCLUSIONS

The reaction zone of nitramine propellant is seen to consist of two characteristic areas: (1) an inner flame area near the solid gas-interface which is at a temperature of  $900 \pm 100$  K and is characterized by the gas-phase reactions of RDX and HCN that provide the heat that determines the burning rate, and (2) an outer flame area farther upstream where NO is converted to  $N_2$  to generate the luminous flame.

## REFERENCES

1. L. E. Harris and M. E. McIlwain, "Coherent Anti-Stokes Raman Spectroscopy in Propellant Flame," Fast Reactions in Energetic Systems, C. Capellos and R. F. Walker, editors, Reidel, Boston, MA, 1981, pp 473-484.
2. L. E. Harris and M. E. McIlwain, Combustion and Flame, vol 48, 1982, p 97.
3. L. E. Harris, Chemical Physics Letters, vol 93, 1982, p 335.
4. L. E. Harris, Combustion and Flame, vol 53, 1983, p 103.
5. K. Aron, L. E. Harris, and J. Fendell, Applied Optics, vol 22, 1983, p 3604.
6. K. Aron and L. E. Harris, Chemical Physics Letters, vol 5, 1984, p 413.
7. L. E. Harris, Chemical Physics Letters, vol 109, 1984, p 112.
8. T. L. Boggs, "The Thermal Behavior of Cyclotrimethylenetrinitramine (RDX) and Cyclotetramethylenetetranitramine (HMX)," Fundamentals of Solid Propellant Combustion, chapter 3, Kenneth K. Kuo and Martin Summerfield, editors, American Institute of Aeronautics and Astronautics, New York, 1984.
9. M. A. Schroeder, "Critical Analysis of Nitramine Decomposition Data Product Distribution from HMX and RDX," Proceedings of the Eighteenth JANNAF Combustion Meeting, Pasadena, CA 1981, pp 299-310.
10. M. Ben-Reuven and L. H. Caveny, "Nitramine Flame and Deflagration Interpreted in Terms of a Flame Model," AIAA Journal, vol 19, 1981, p 1276.
11. M. Ben-Reuven and M. Summerfield, "Combustion of Nitramine Propellants," Contractor Report ARBRL-CR-00507, ARRADCOM, Aberdeen Proving Ground, MD, March 1983.
12. N. Kubota, "Combustion Mechanisms of Nitramine Composite Propellants," Eighteenth Symposium on Combustion, 1981, p 187.
13. C. F. Price, T. L. Boggs, T. P. Parr, and D. M. Parr, "A Modified BDP Model Applied to the Self-Deflagration of HMX," Proceedings of Nineteenth JANNAF Combustion Meeting, 1982, pp 299-310.
14. N. S. Cohen, G. A. Lo, and J. C. Crowley, AIAA Journal, vol 23, 1985, p 276.
15. M. S. Miller, Combustion and Flame, vol 46, 1982, p 51.
16. M. S. Miller and T. P. Coffee, Combustion and Flame, vol 50, 1983, pp 65 and 75.
17. Sylvia A. J. Druet and Jean-Pierre E. Taran, Progress in Quantum Electronics, vol 7, 1981, p 1.

18. A. C. Ecbreth and P. Schreiber, "Coherent Anti-Stokes Raman Spectroscopy (CARS), Chemical Applications of Nonlinear Raman Spectroscopy, A. B. Harvey, editor, Academic Press, New York, 1981, p 27.
19. W. C. Gardner, Combustion Chemistry, Springer-Verlag, New York, 1984.
20. W. M. Tolles, J. W. Nibler, J. R. McDonald, and A. B. Harvey, Applied Spectroscopy, vol 31, 1977, p 253.
21. R. J. Hall, Combustion and Flame, vol 35, 1979, p 47.
22. S. Gordon and B. J. McBride, NASA-Lewis Report SP 273, 1976.
23. L. E. Harris, Chemical Physics Letters, vol 93, 1982, p 335.
24. L. E. Harris, Combustion and Flame, vol 53, 1983, p 103.
25. J. P. Champion and J. Berger, J. Physique, vol 36, 1975, p 135.
26. D. L. Gray and A. G. Robiette, Molecular Physics, vol 32, 1976, p 1609.
27. G. Herzberg, Infrared and Raman Spectra, Van Nostrand Reinhold Co., New York, p 278.
28. R. H. Hunt, J. E. Lolck, A. G. Robiette, L. R. Brown, and R. A. Toth, Molecular Spectry, vol 92, 1982, p 246.
29. J. Fendell, L. E. Harris, and K. Aron, "Theoretical Calculation of H<sub>2</sub> CARS Spectra for Propellant Flames," Technical Report ARLCD-TR-83048, ARDC, Dover, NJ, December 1983.
30. I. Dabrowski, Canadian Journal of Physics, vol 62, 1984, p 1637.
31. T. Haw, W. Y. Cheung, G. C. Baumann, D. Chiu, and L. E. Harris, "A Study of Flame Species Using CARS," Abstract WH10, Proceedings of Fortieth Symposium on Molecular Spectroscopy, Ohio State University, Columbus, OH, to be published.
32. Z. Iqbal, K. Suryanarayana, S. Bulusu, and Jr. R. Autera, "Infrared and Raman Spectra of 1,3,5-Trinitro-1,3,5-Triazacyclohexane (RDX)," Technical Report 4401, Picatinny Arsenal, Dover, NJ, October 1972.
33. V. P. Balakhnine Vandooren and P. J. Van Tiggelen, Combustion and Flame, vol 28, 1977, p 165.
34. K. Tabayaski and S. H. Bauer, Combustion and Flame, vol 34, 1979, p 63.
35. S. S. Wagel, T. Carrington, S. V. Filseth, and C. M. Sadowski, Chemical Physics Letters, vol 69, 1982, p 61.
36. C. K. Westbrook and F. L. Dryer, Progress in Energy and Combustion Science, 1984, pl.

37. M. P. Zabielski, "Mechanism and Reaction Dynamics Related to Methane Combustion," Report No. 956114-25, United Technology Research Center, East Hartford, CT, 1984.
38. R. A. Perry and C. F. Melius, "The Rate of the Reaction of HCN with Oxygen Atoms over the Temperature Range 540-900 K," presented at the Twentieth Symposium (International) on Combustion, University of Michigan, Ann Arbor, MI, July 1984.
39. J. A. Miller, M. C. Branch, W. J. McLean, D. W. Chandler, D. S. Mitchell, and R. J. Kee, "The Conversion of HCN to NO and N<sub>2</sub> in H<sub>2</sub>-O<sub>2</sub>-HCN-Ar Flames at Low Pressure," Report WSS/CT 84-36, Sandia National Laboratories, Livermore, CA, 1984.
40. J. A. Miller, M. D. Smooke, R. M. Green, and R. J. Kee, Combustion Science and Technology, vol 34, 1983, p 149.
41. D. L. Baulch, D. D. Drydale, and D. G. Horne, Evaluated Kinetic Data for High Temperature Reactions, vol 2, Butterworths, London, 1973.

Table 1. Laser dyes

Dye	Solvent	Concentration ( $\times 10^5$ M)		Nonresonant background		Species observed																																																																																																				
		Oscillator	Amplifier	$I_{\max}$ ( $\text{cm}^{-2}$ )	FWHM ( $\text{cm}^{-1}$ )																																																																																																					
DCM	EtOH	5.8	0.6	4210	300	$\text{H}_2(\text{g})$																																																																																																				
LDS698		2.0	2.0				DCM	EtOH	25	8.4	3930	420	$\text{H}_2(\text{g})$ $\text{H}_2\text{O}$	LDS698	16	5.4	Rh640	MeOH (NaOH)	44.5	4.1	3920	150	$\text{H}_2(\text{g})$ $\text{N}_2$	Ox725	7.8	1.5	2270	110	LD690	MeOH	25	8.3	3390	80	$\text{CH}_4$ overtones		3225	70	LD690	MeOH	15	8.3	3190	95	$\text{CH}_4$ overtones	Rh640	MeOH	24	3.2	2300	110	$\text{N}_2$ , $\text{N}_2\text{O}$	Kiton red	MeOH	10	10	2180	150	$\text{N}_2\text{O}$ , CO, HCN, $\text{H}_2(\text{s})$	Rh640	3	3	Kiton red	MeOH	21	2.8	1860	100	$\text{NO}$ , $\text{H}_2(\text{s})$	Rh640	4.5	0.3	Kiton red	MeOH	21	2.8	1820	110	$\text{NO}$ , $\text{H}_2(\text{s})$ , $\text{O}_2$	Rh640	2.8	0	Kiton red	MeOH	23	2.8	1730	110	$\text{H}_2(\text{s})$ , $\text{O}_2$ , $\text{CH}_4(\text{s})$	Kiton red	EtOH	23	2.8	1660		$\text{O}_2$ , $\text{CH}_4(\text{s})$	Rh610	MeOH with 4 drops saturated NaOH	21	3.7	1540	110	$\text{CH}_4$ , $\text{H}_2(\text{s})$ , $\text{CO}_2$ , $\text{O}_2$		EtOH with aqueous NaOH	
DCM	EtOH	25	8.4	3930	420	$\text{H}_2(\text{g})$ $\text{H}_2\text{O}$																																																																																																				
LDS698		16	5.4				Rh640	MeOH (NaOH)	44.5	4.1	3920	150	$\text{H}_2(\text{g})$ $\text{N}_2$	Ox725	7.8	1.5	2270	110	LD690	MeOH	25	8.3	3390	80	$\text{CH}_4$ overtones		3225	70	LD690	MeOH	15	8.3	3190	95	$\text{CH}_4$ overtones	Rh640	MeOH	24	3.2	2300	110	$\text{N}_2$ , $\text{N}_2\text{O}$	Kiton red	MeOH	10	10	2180	150	$\text{N}_2\text{O}$ , CO, HCN, $\text{H}_2(\text{s})$	Rh640	3	3	Kiton red	MeOH	21	2.8	1860	100	$\text{NO}$ , $\text{H}_2(\text{s})$	Rh640	4.5	0.3	Kiton red	MeOH	21	2.8	1820	110	$\text{NO}$ , $\text{H}_2(\text{s})$ , $\text{O}_2$	Rh640	2.8	0	Kiton red	MeOH	23	2.8	1730	110	$\text{H}_2(\text{s})$ , $\text{O}_2$ , $\text{CH}_4(\text{s})$	Kiton red	EtOH	23	2.8	1660		$\text{O}_2$ , $\text{CH}_4(\text{s})$	Rh610	MeOH with 4 drops saturated NaOH	21	3.7	1540	110	$\text{CH}_4$ , $\text{H}_2(\text{s})$ , $\text{CO}_2$ , $\text{O}_2$		EtOH with aqueous NaOH			1335	100	$\text{CO}_2$ , $\text{H}_2(\text{s})$ , $\text{N}_2\text{O}$						
Rh640	MeOH (NaOH)	44.5	4.1	3920	150	$\text{H}_2(\text{g})$ $\text{N}_2$																																																																																																				
Ox725		7.8	1.5	2270	110		LD690	MeOH	25	8.3	3390	80	$\text{CH}_4$ overtones		3225	70	LD690	MeOH	15	8.3	3190	95	$\text{CH}_4$ overtones	Rh640	MeOH	24	3.2	2300	110	$\text{N}_2$ , $\text{N}_2\text{O}$	Kiton red	MeOH	10	10	2180	150	$\text{N}_2\text{O}$ , CO, HCN, $\text{H}_2(\text{s})$	Rh640	3	3	Kiton red	MeOH	21	2.8	1860	100	$\text{NO}$ , $\text{H}_2(\text{s})$	Rh640	4.5	0.3	Kiton red	MeOH	21	2.8	1820	110	$\text{NO}$ , $\text{H}_2(\text{s})$ , $\text{O}_2$	Rh640	2.8	0	Kiton red	MeOH	23	2.8	1730	110	$\text{H}_2(\text{s})$ , $\text{O}_2$ , $\text{CH}_4(\text{s})$	Kiton red	EtOH	23	2.8	1660		$\text{O}_2$ , $\text{CH}_4(\text{s})$	Rh610	MeOH with 4 drops saturated NaOH	21	3.7	1540	110	$\text{CH}_4$ , $\text{H}_2(\text{s})$ , $\text{CO}_2$ , $\text{O}_2$		EtOH with aqueous NaOH			1335	100	$\text{CO}_2$ , $\text{H}_2(\text{s})$ , $\text{N}_2\text{O}$																		
LD690	MeOH	25	8.3	3390	80	$\text{CH}_4$ overtones																																																																																																				
				3225	70		LD690	MeOH	15	8.3	3190	95	$\text{CH}_4$ overtones	Rh640	MeOH	24	3.2	2300	110	$\text{N}_2$ , $\text{N}_2\text{O}$	Kiton red	MeOH	10	10	2180	150	$\text{N}_2\text{O}$ , CO, HCN, $\text{H}_2(\text{s})$	Rh640	3	3	Kiton red	MeOH	21	2.8	1860	100	$\text{NO}$ , $\text{H}_2(\text{s})$	Rh640	4.5	0.3	Kiton red	MeOH	21	2.8	1820	110	$\text{NO}$ , $\text{H}_2(\text{s})$ , $\text{O}_2$	Rh640	2.8	0	Kiton red	MeOH	23	2.8	1730	110	$\text{H}_2(\text{s})$ , $\text{O}_2$ , $\text{CH}_4(\text{s})$	Kiton red	EtOH	23	2.8	1660		$\text{O}_2$ , $\text{CH}_4(\text{s})$	Rh610	MeOH with 4 drops saturated NaOH	21	3.7	1540	110	$\text{CH}_4$ , $\text{H}_2(\text{s})$ , $\text{CO}_2$ , $\text{O}_2$		EtOH with aqueous NaOH			1335	100	$\text{CO}_2$ , $\text{H}_2(\text{s})$ , $\text{N}_2\text{O}$																												
LD690	MeOH	15	8.3	3190	95	$\text{CH}_4$ overtones																																																																																																				
Rh640	MeOH	24	3.2	2300	110	$\text{N}_2$ , $\text{N}_2\text{O}$																																																																																																				
Kiton red	MeOH	10	10	2180	150	$\text{N}_2\text{O}$ , CO, HCN, $\text{H}_2(\text{s})$																																																																																																				
Rh640		3	3				Kiton red	MeOH	21	2.8	1860	100	$\text{NO}$ , $\text{H}_2(\text{s})$	Rh640	4.5	0.3	Kiton red	MeOH	21	2.8	1820	110	$\text{NO}$ , $\text{H}_2(\text{s})$ , $\text{O}_2$	Rh640	2.8	0	Kiton red	MeOH	23	2.8	1730	110	$\text{H}_2(\text{s})$ , $\text{O}_2$ , $\text{CH}_4(\text{s})$	Kiton red	EtOH	23	2.8	1660		$\text{O}_2$ , $\text{CH}_4(\text{s})$	Rh610	MeOH with 4 drops saturated NaOH	21	3.7	1540	110	$\text{CH}_4$ , $\text{H}_2(\text{s})$ , $\text{CO}_2$ , $\text{O}_2$		EtOH with aqueous NaOH			1335	100	$\text{CO}_2$ , $\text{H}_2(\text{s})$ , $\text{N}_2\text{O}$																																																				
Kiton red	MeOH	21	2.8	1860	100	$\text{NO}$ , $\text{H}_2(\text{s})$																																																																																																				
Rh640		4.5	0.3				Kiton red	MeOH	21	2.8	1820	110	$\text{NO}$ , $\text{H}_2(\text{s})$ , $\text{O}_2$	Rh640	2.8	0	Kiton red	MeOH	23	2.8	1730	110	$\text{H}_2(\text{s})$ , $\text{O}_2$ , $\text{CH}_4(\text{s})$	Kiton red	EtOH	23	2.8	1660		$\text{O}_2$ , $\text{CH}_4(\text{s})$	Rh610	MeOH with 4 drops saturated NaOH	21	3.7	1540	110	$\text{CH}_4$ , $\text{H}_2(\text{s})$ , $\text{CO}_2$ , $\text{O}_2$		EtOH with aqueous NaOH			1335	100	$\text{CO}_2$ , $\text{H}_2(\text{s})$ , $\text{N}_2\text{O}$																																																														
Kiton red	MeOH	21	2.8	1820	110	$\text{NO}$ , $\text{H}_2(\text{s})$ , $\text{O}_2$																																																																																																				
Rh640		2.8	0				Kiton red	MeOH	23	2.8	1730	110	$\text{H}_2(\text{s})$ , $\text{O}_2$ , $\text{CH}_4(\text{s})$	Kiton red	EtOH	23	2.8	1660		$\text{O}_2$ , $\text{CH}_4(\text{s})$	Rh610	MeOH with 4 drops saturated NaOH	21	3.7	1540	110	$\text{CH}_4$ , $\text{H}_2(\text{s})$ , $\text{CO}_2$ , $\text{O}_2$		EtOH with aqueous NaOH			1335	100	$\text{CO}_2$ , $\text{H}_2(\text{s})$ , $\text{N}_2\text{O}$																																																																								
Kiton red	MeOH	23	2.8	1730	110	$\text{H}_2(\text{s})$ , $\text{O}_2$ , $\text{CH}_4(\text{s})$																																																																																																				
Kiton red	EtOH	23	2.8	1660		$\text{O}_2$ , $\text{CH}_4(\text{s})$																																																																																																				
Rh610	MeOH with 4 drops saturated NaOH	21	3.7	1540	110	$\text{CH}_4$ , $\text{H}_2(\text{s})$ , $\text{CO}_2$ , $\text{O}_2$																																																																																																				
	EtOH with aqueous NaOH			1335	100	$\text{CO}_2$ , $\text{H}_2(\text{s})$ , $\text{N}_2\text{O}$																																																																																																				

Table 2. Summary of species identified in a  $\phi = 3.2$   $\text{CH}_4/\text{N}_2\text{O}$  flame

<u>Observed <math>I_{\text{max}}</math> (<math>\text{cm}^{-1}</math>)</u>	<u>Species</u>	<u>Comment</u>
4155-4075	$\text{H}_2$ Q-branch	Temperature calculations indicate a temperature of 500 K in preheat zone.
3240-3100	$\text{CH}_4$ ( $2 \nu_2$ )	Rapid decrease in reaction zone
2325	$\text{N}_2$	Gradual increase in reaction zone
2222	$\text{N}_2\text{O}$ ( $\nu_3$ )	Rapid decrease in reaction zone
2136	CO	Increase in reaction zone
2129	$\text{H}_2$ S(9)	Rapid increase of intensity in reaction zone; large compared to CO
1813	$\text{H}_2$ S(7)	Signal intensity increases up the reaction zone
1636	$\text{H}_2$ S(6)	Weak signal seen in post flame
1531	$\text{CH}_4$ ( $\nu_2$ )	Gradual decrease in reaction zone
1447	$\text{H}_2$ S(5)	Signal intensity increases up the reaction zone
1294	$\text{N}_2\text{O}$ ( $\nu_1$ )	Intense signal that decreases rapidly in reaction zone

Table 3. Summary of species identified in nitramine propellant flame

<u>Observed <math>I_{\max}</math> (<math>\text{cm}^{-1}</math>)</u>	<u>Species</u>	<u>Comment</u>
4155-4075	H <sub>2</sub> Q - branch	Temperature calculations indicate a temperature of 900 K at the surface of the propellant
2325	N <sub>2</sub>	Slow increase until near the end of reaction zone, a large increase occurs
2136	CO	Signal increases up reaction zone
2129	H <sub>2</sub> S(9)	Observed similar intensity to CO
2086	HCN ( $\nu_1$ )*	Strong signal initially which diminishes rapidly
1872	NO	Low concentration modulation which remains constant throughout reaction zone; decreases rapidly at end of reaction zone
1814	H <sub>2</sub> S(7)	Signal intensity increases up the reaction zone
1599	RDX (NO <sub>2</sub> asymmetric stretch)*	Moderate concentration early in the reaction zone
1447	H <sub>2</sub> S(5)	Signal intensity increases up the reaction zone
1387	CO <sub>2</sub> ( $\nu_1$ )	Moderate signal early in reaction

---

\* Tentative.

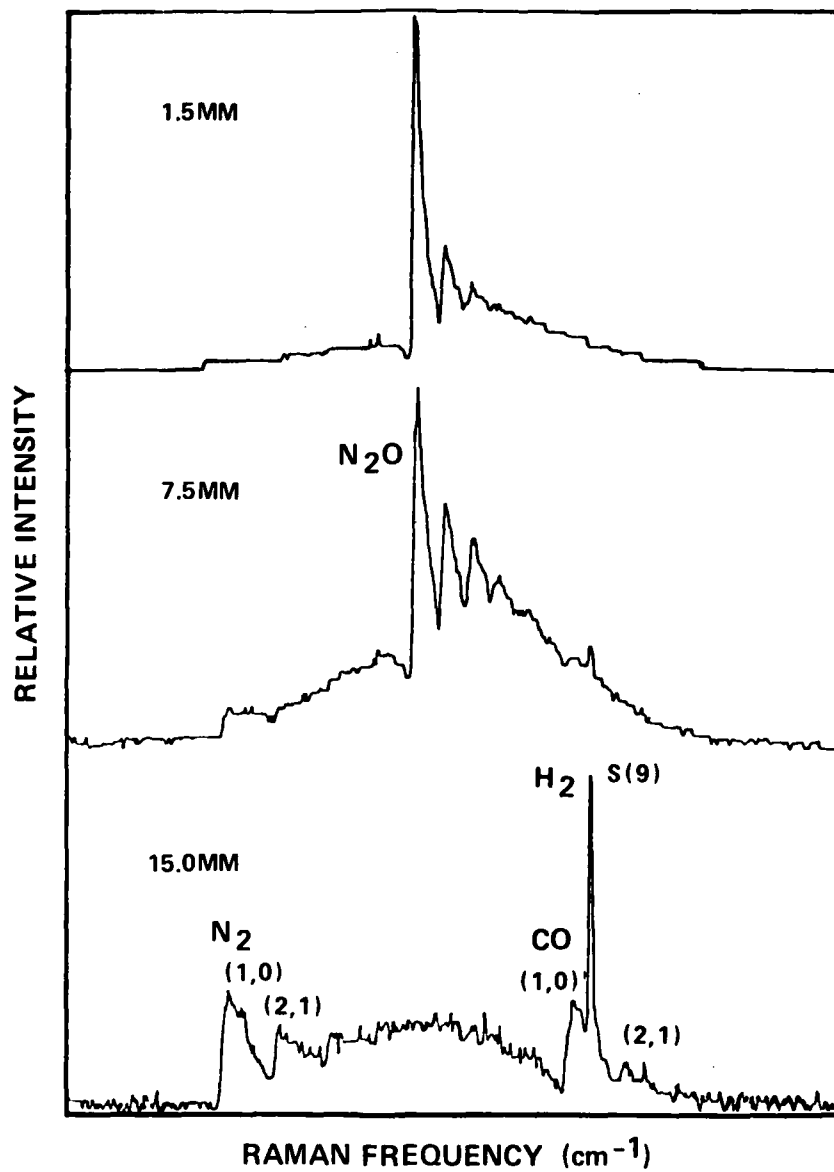


Figure 1. CARS spectra of N<sub>2</sub>O, CO, N<sub>2</sub>, and H<sub>2</sub> S(9) from a  $\phi = 3.2$  CH<sub>4</sub>/N<sub>2</sub>O flame

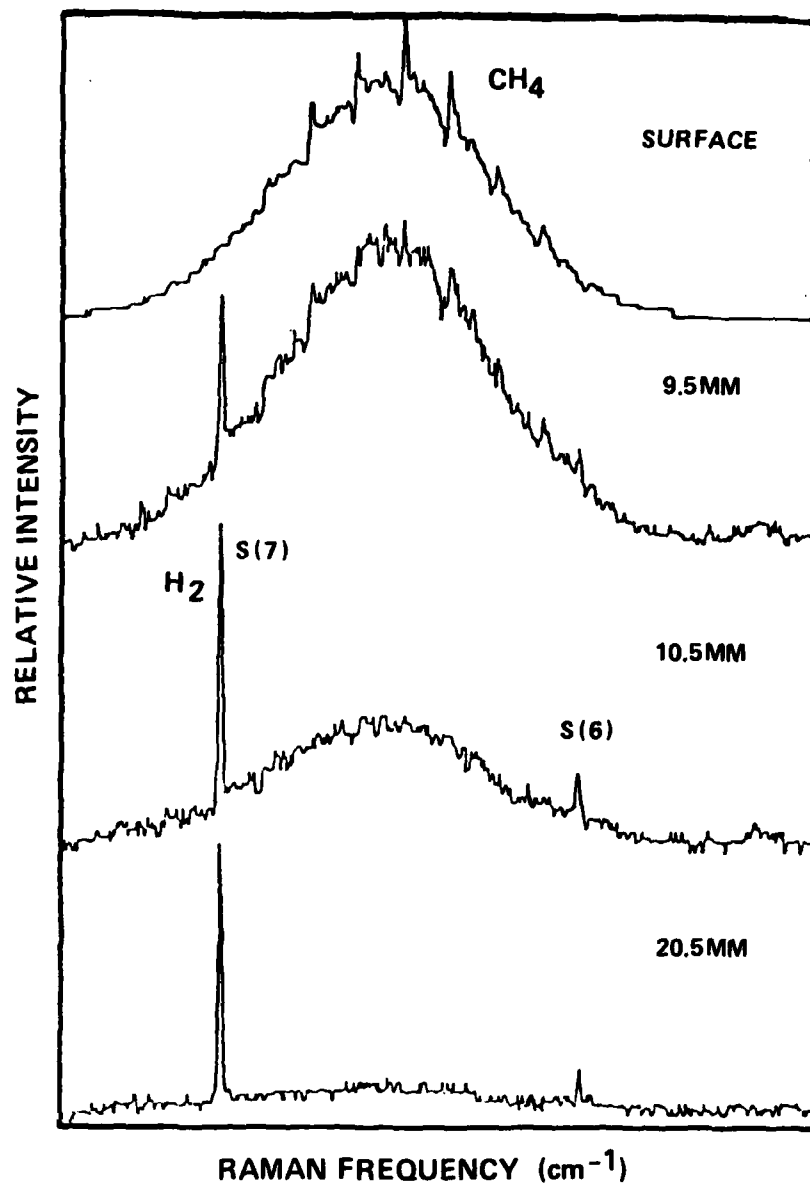


Figure 2a. CARS spectra of CH<sub>4</sub> ( $\nu_2$ ) and H<sub>2</sub> S(7) and S(6) from a  $\phi$  3.2 CH<sub>4</sub>/N<sub>2</sub>O flame

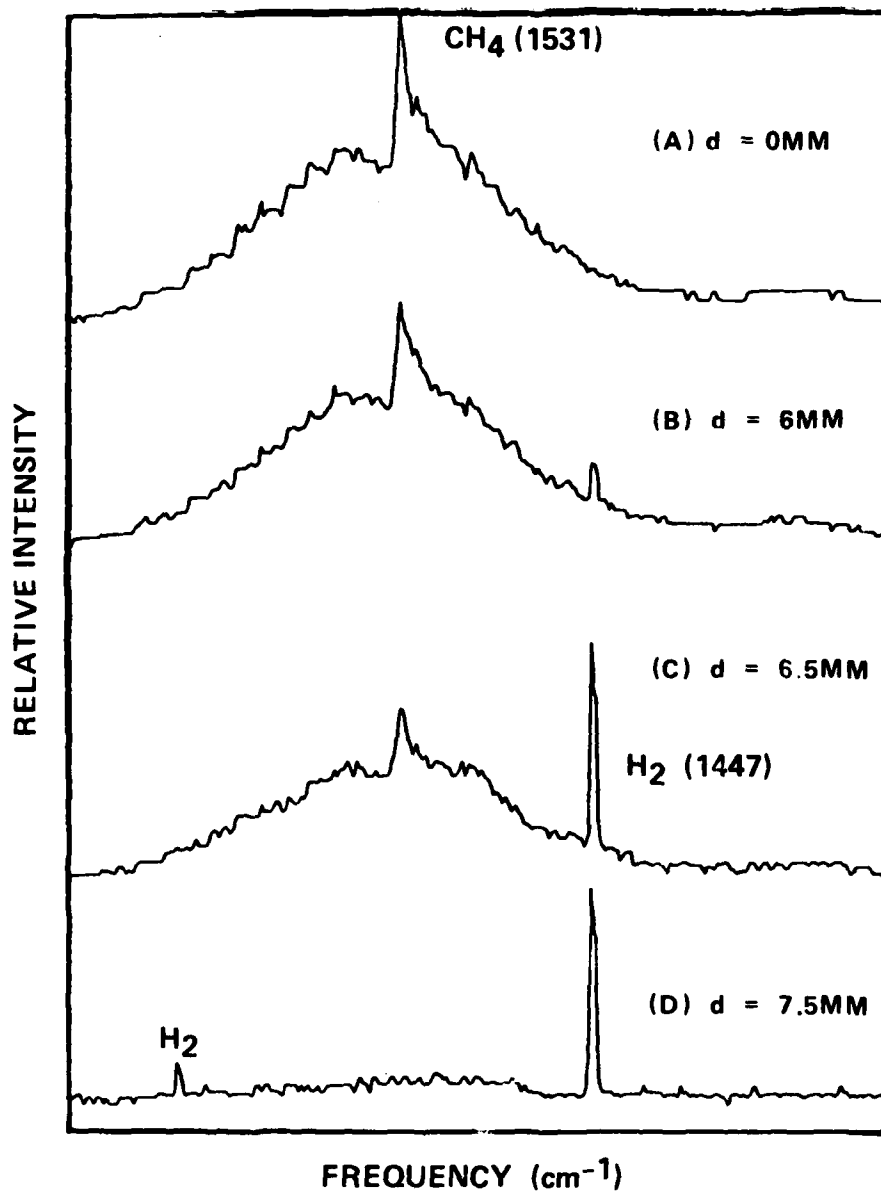


Figure 2b. CARS spectra of  $\text{CH}_4$  ( $\nu_2$ ) and  $\text{H}_2$  S(5) and S(6) from a  $\phi = 3.2$   $\text{CH}_4/\text{N}_2\text{O}$  flame

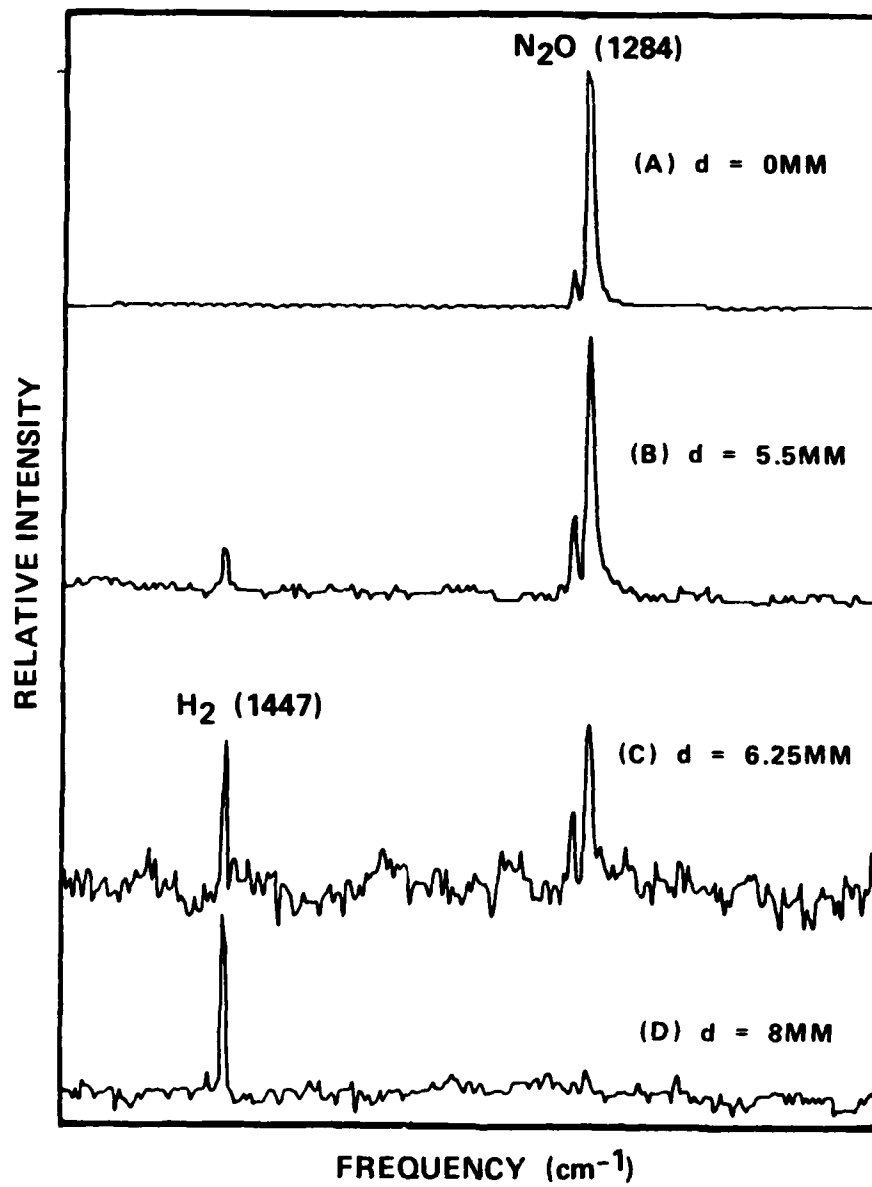


Figure 3. CARS spectra of  $\text{N}_2\text{O}$  and  $\text{H}_2 \text{ S}(5)$  from a  $\phi = 3.2$   $\text{CH}_4/\text{N}_2\text{O}$  flame

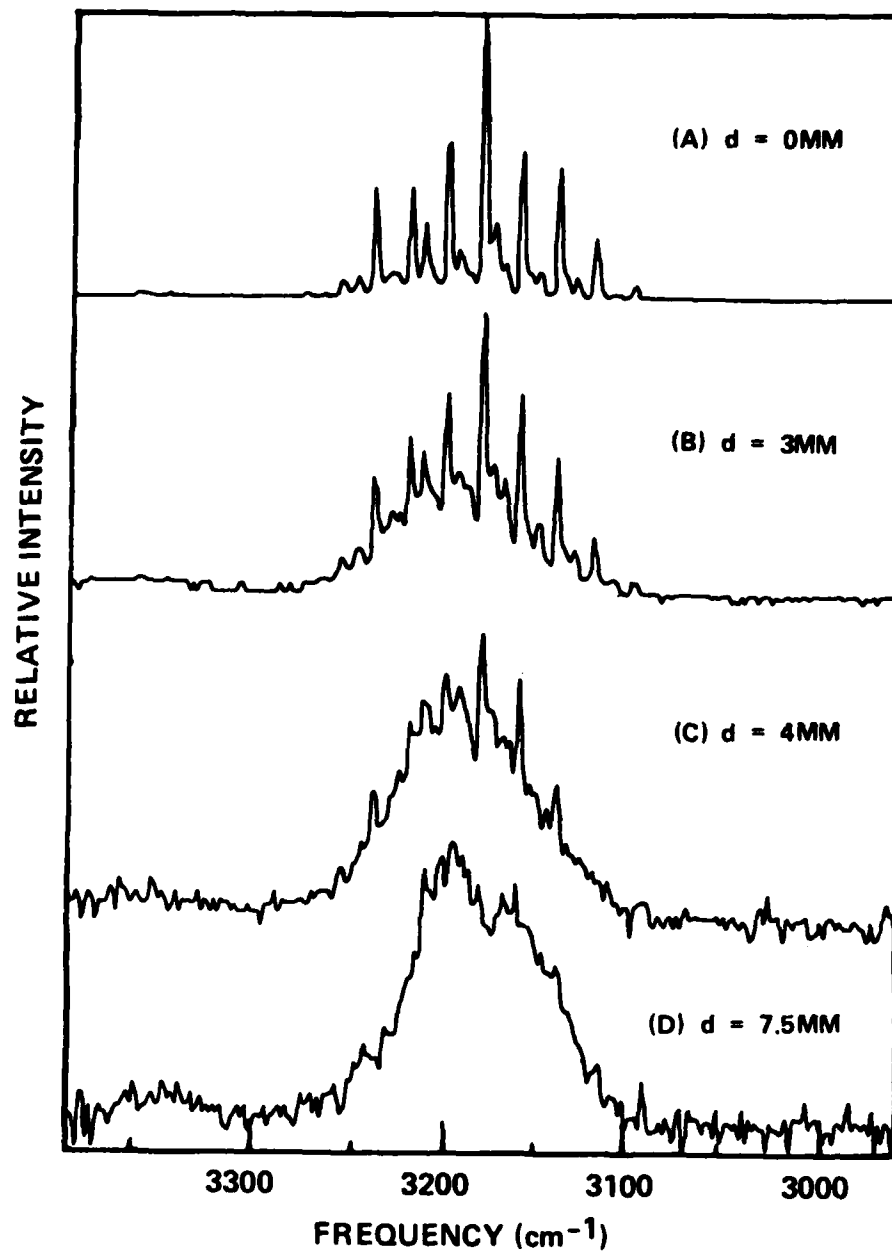


Figure 4. CARS spectra of  $\text{CH}_4$  ( $2\nu_2$ ) from a  $\phi = 3.2$   $\text{CH}_4/\text{N}_2\text{O}$  flame

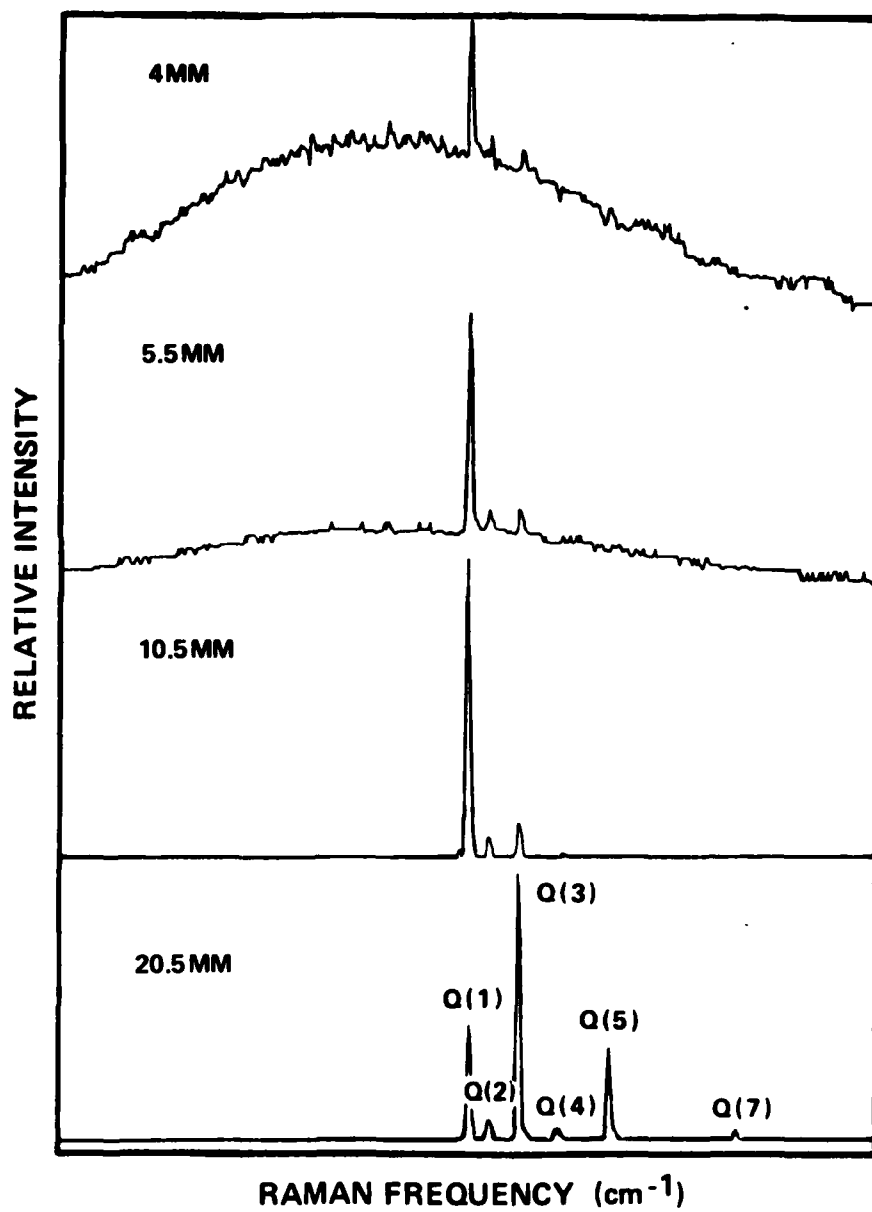


Figure 5. CARS spectra of H<sub>2</sub> Q-branch ( $v'' = 0$ ) in a  $\phi = 3.2$  CH<sub>4</sub>/N<sub>2</sub>O flame

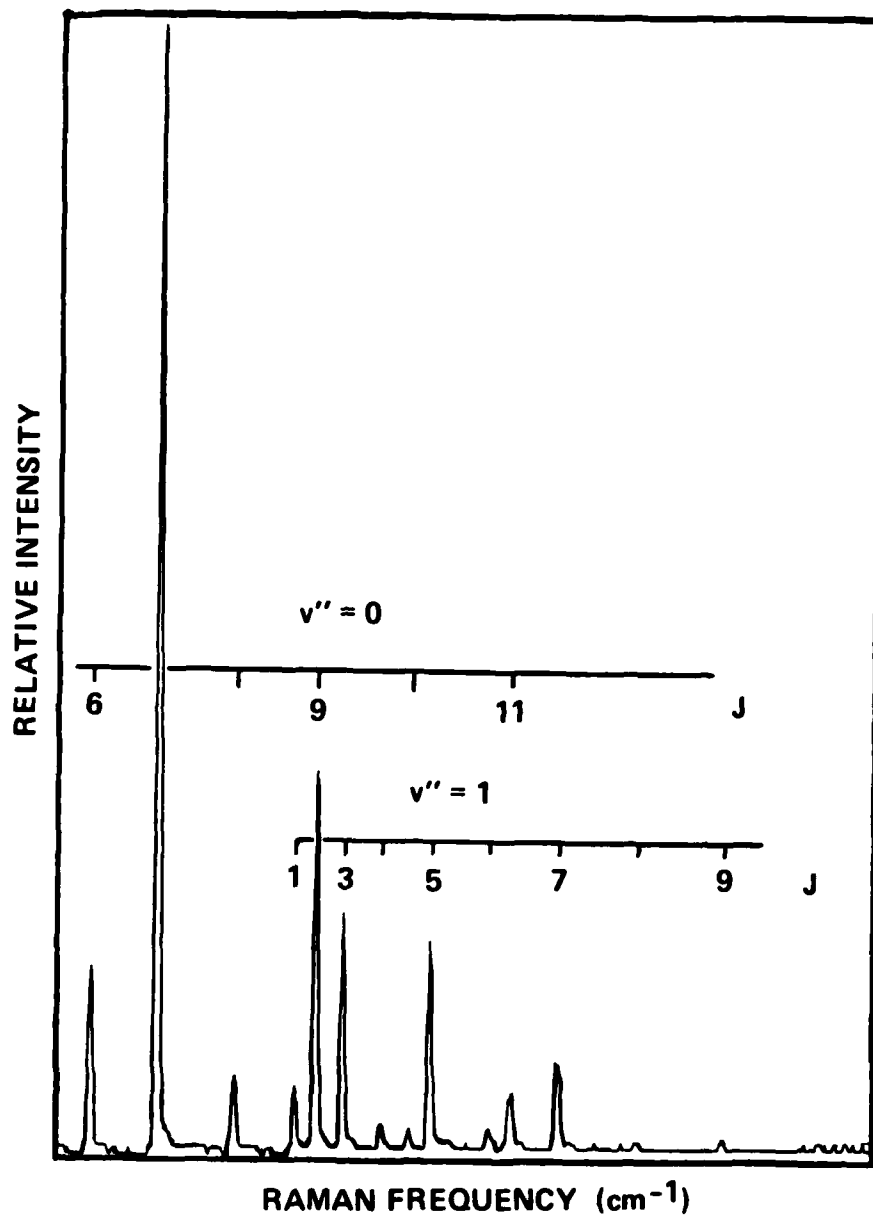


Figure 6. CARS spectra of H<sub>2</sub> Q-branch ( $v'' = 0$  and  $v'' = 1$ ) in a  $\phi = 1.8$  CH<sub>4</sub>/N<sub>2</sub>O flame

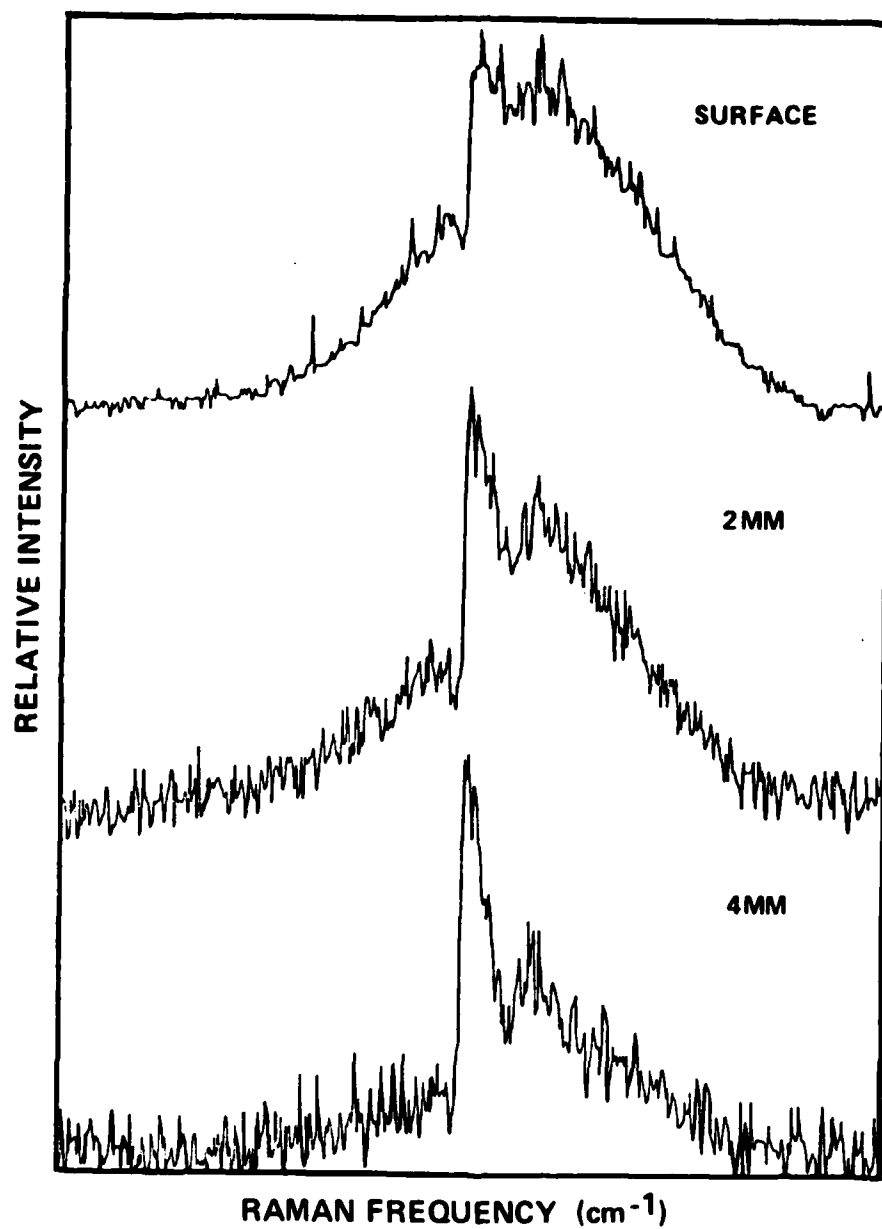


Figure 7. Time-averaged CARS spectra of  $N_2$  at various distances above the surface of a nitramine propellant flame

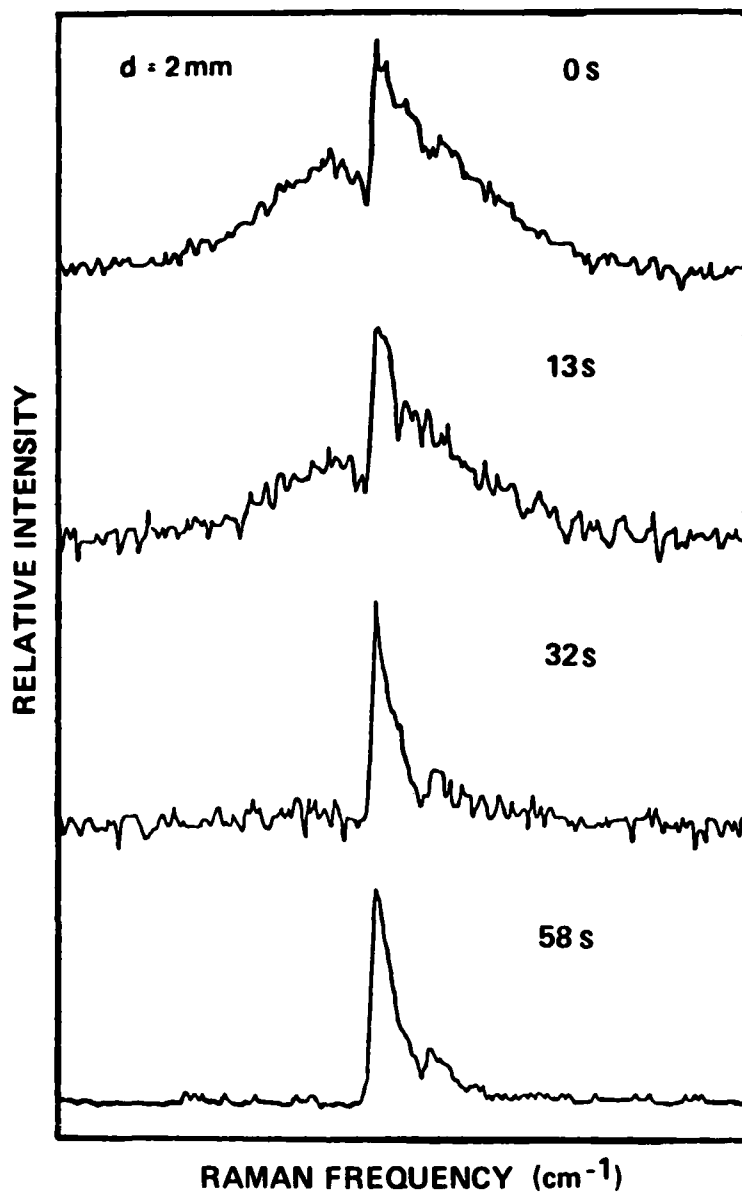


Figure 8. Time-resolved CARS spectra of  $N_2$  at various times after ignition at 2-mm above the surface of a nitramine propellant

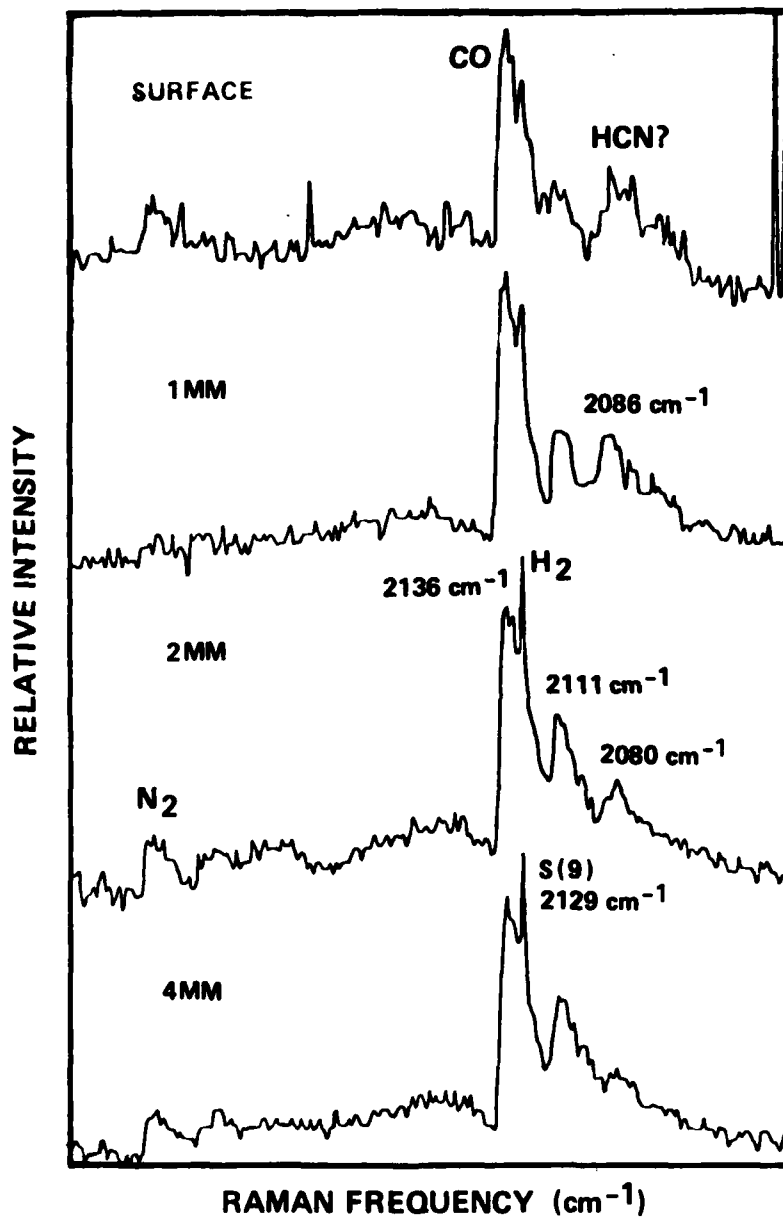
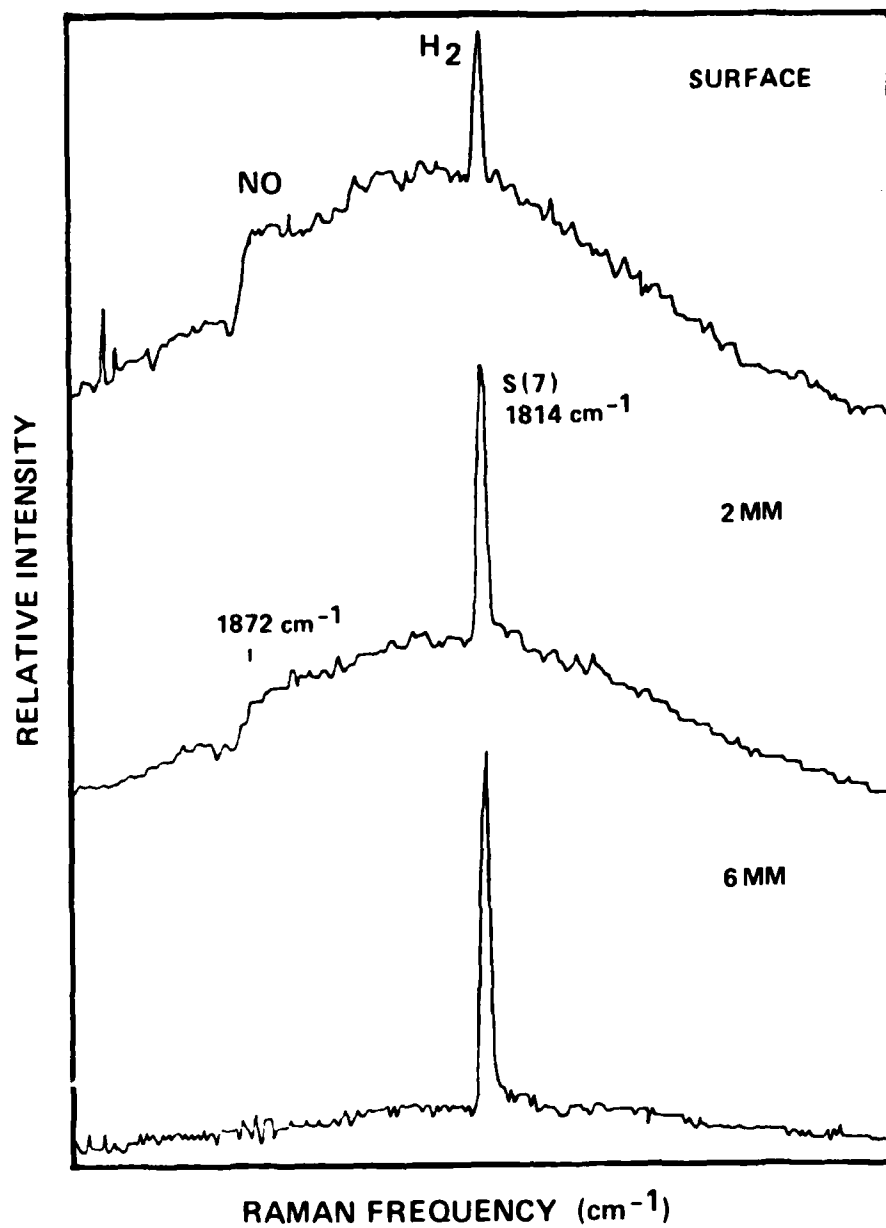
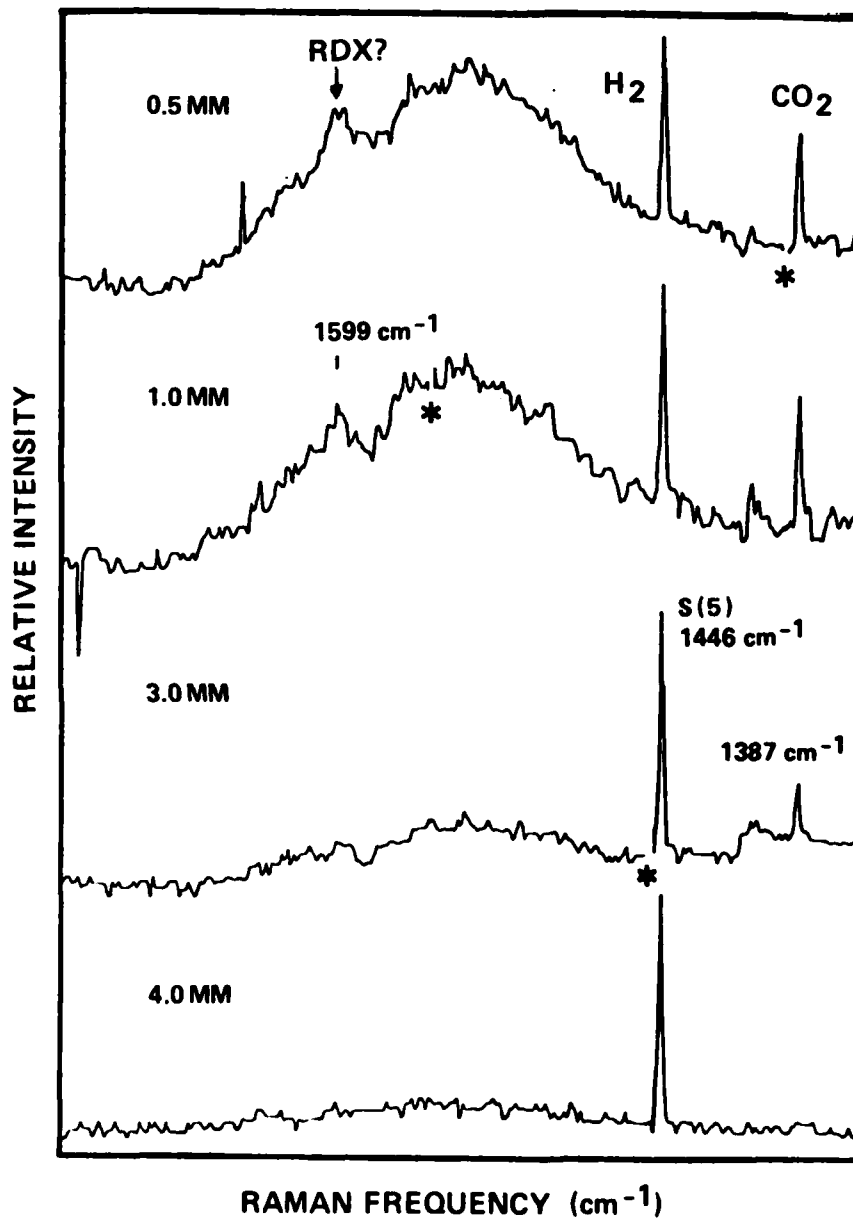


Figure 9. Time-averaged CARS spectra of HCN, CO, N<sub>2</sub>, and H<sub>2</sub> S(9) above the surface of a nitramine propellant flame

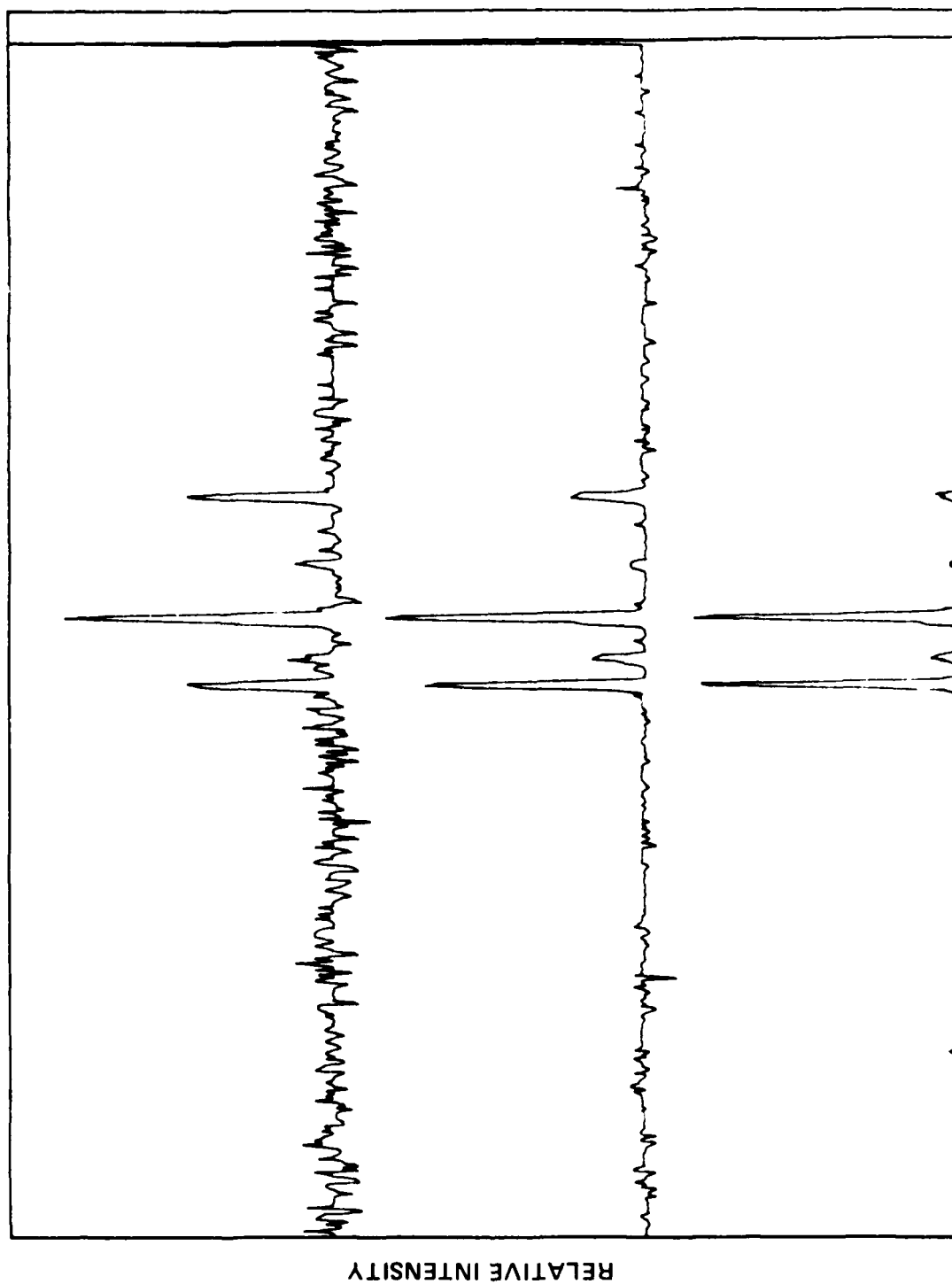


10. Time-averaged CARS spectra of NO and H<sub>2</sub> S(7) above the surface of a nitramine propellant



\* FOR CLARITY, SPIKES DUE TO ARCING NEAR THE PROPELLANT SURFACE HAVE BEEN REMOVED.

Figure 11. Time-averaged CARS spectra of RDX (tentative), H<sub>2</sub> S(5), and CO<sub>2</sub> above the surface of a nitramine propellant



RAMAN FREQUENCY ( $\text{cm}^{-1}$ )

Figure 12. Time-resolved (single shot) CARS spectra of the  $\text{H}_2$  Q branch taken at nominal 6-second intervals after ignition, and shown sequentially from bottom to top

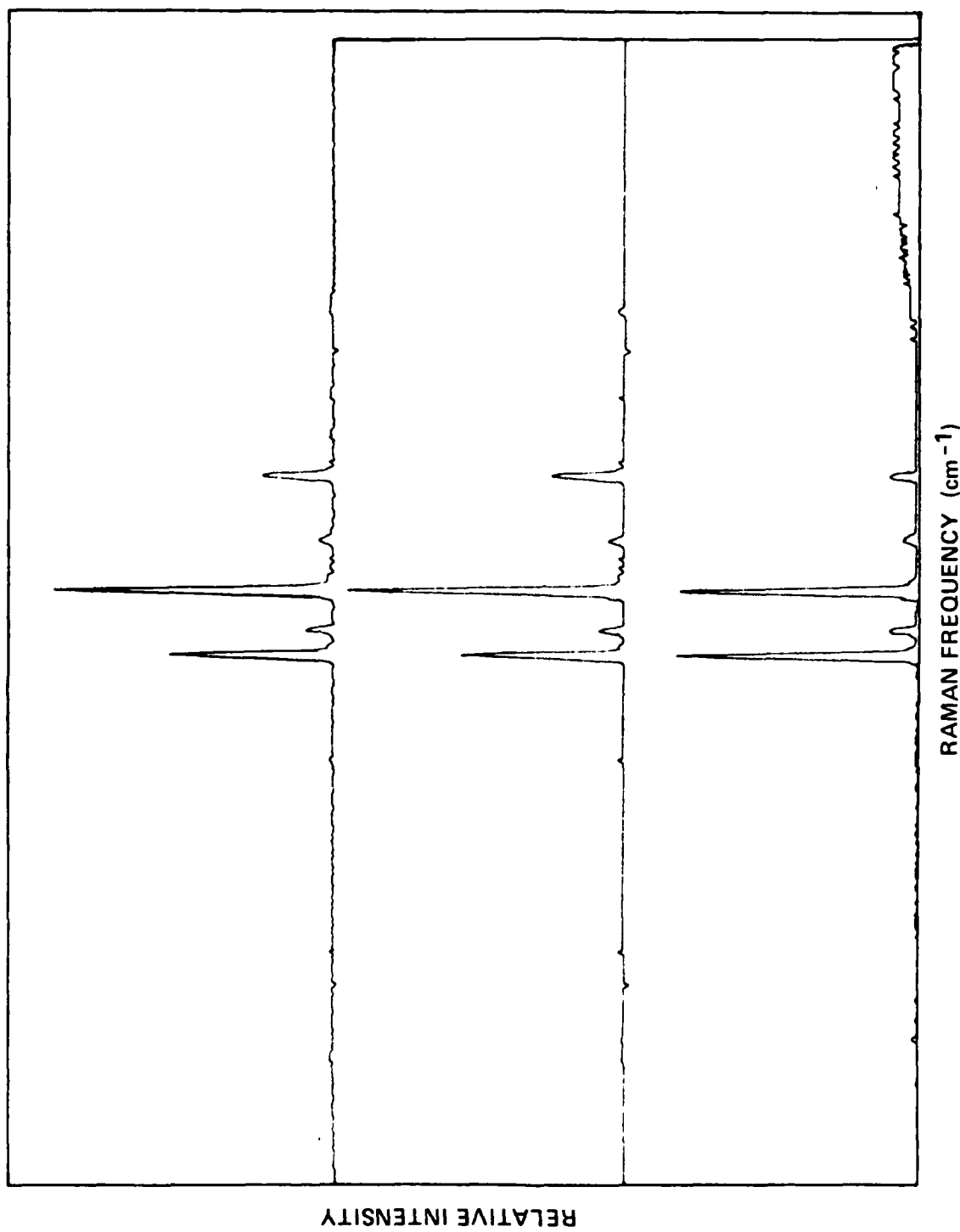


Figure 13. Time-resolved (10-shot averaged) CARS spectra of the H<sub>2</sub> Q branch taken at nominal 6-second intervals after ignition and shown sequentially from bottom to top

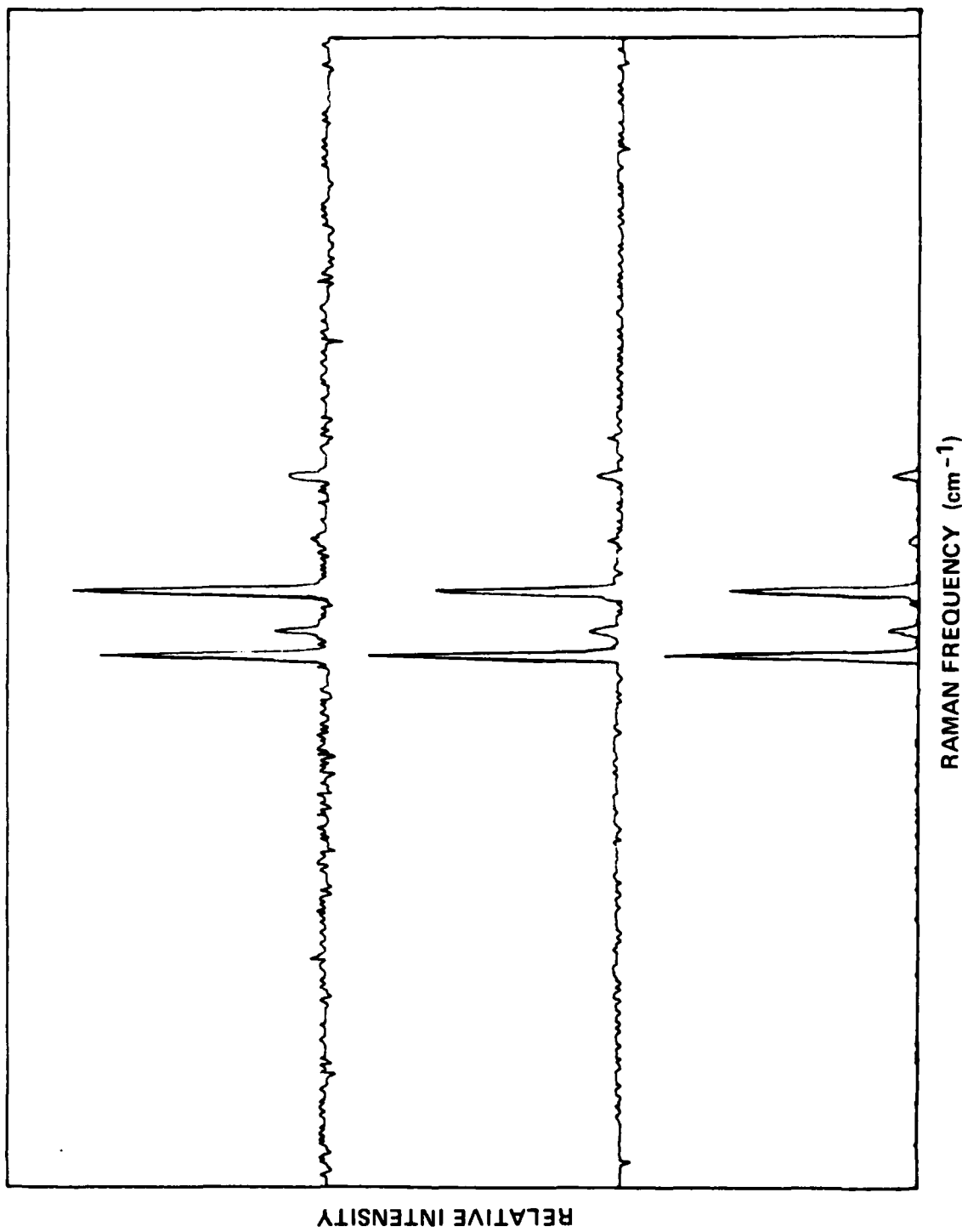


Figure 14. Time-resolved (3-shot averaged) CARS spectra of the H<sub>2</sub> Q branch taken at nominal 6-second intervals after ignition and shown sequentially from bottom to top

DISTRIBUTION LIST

Commander  
Armament Research and Development Center  
U.S. Army Armament, Munitions  
and Chemical Command  
ATTN: SMCAR-TD, A. Moss  
SMCAR-TDC, H. Grundler  
SMCAR-AE, R. Bushey  
P. Picard  
SMCAR-AEE, J. Lannon  
SMCAR-AEE-WE, F. Gilbert  
SMCAR-AEE-WW, S. Bulusu  
SMCAR-AEE-WW, C. Capellos  
SMCAR-AEE-WW, F. Owens  
SMCAR-AEP, D. Downs  
SMCAR-AEP-R, L. Harris (10)  
SMCAR-AEP-R, A. Beardell  
SMCAR-AEP-R, B. Brodman  
SMCAR-AEP-R, Y. Carignon  
SMCAR-AEP-R, L. Stiefel  
SMCAR-AEP-R, T. Vladimiroff  
SMCAR-AER-T, P. Marinkas  
SMCAR-MSI (5)  
Dover, NJ 07801-5001

Commander  
U.S. Army Armament, Munitions  
and Chemical Command  
ATTN: AMSMC-GCL(D)  
AMSMC-QAH-T, J. Moskowitz  
J. M. Argento  
Dover, NJ 07801-5001

Administrator  
Defense Technical Information Center  
ATTN: Accessions Division (12)  
Cameron Station  
Alexandria, VA 22304-6145

Director  
U.S. Army Materiel Systems  
Analysis Activity  
ATTN: AMXSY-MP  
Aberdeen Proving Ground, MD 21005-5066

Commander  
Chemical Research and Development Center  
U.S. Army Armament, Munitions  
and Chemical Command  
ATTN: SMCCR-SPS-IL  
Aberdeen Proving Ground, MD 21010-5423

Commander  
Chemical Research and Development Center  
U.S. Army Armament, Munitions  
and Chemical Command  
ATTN: SMCCR-RSP-A  
Aberdeen Proving Ground, MD 21010-5423

Director  
Ballistic Research Laboratory  
ATTN: AMXBR-OD-ST  
SLCBR-IB, L. Watermier  
A. Barrows  
G. Adams  
R. Fifer  
M. Miller  
T. Coffee  
J. Heimeryl  
C. Nelson  
J. Vanderhoff  
J. Anderson

Aberdeen Proving Ground, MD 21005-5066

Chief  
Benet Weapons Laboratory, CCAC  
Armament Research and Development Center  
U.S. Army Armament, Munitions  
and Chemical Command  
ATTN: SMCAR-CCB-TL  
Watervliet, NY 12189-5000

Commander  
U.S. Army Armament, Munitions  
and Chemical Command  
ATTN: AMSMC-ESP-L  
Rock Island, IL 61299-6000

Director  
U.S. Army TRADOC Systems  
Analysis Activity  
ATTN: ATAA-SL  
White Sands Missile Range, NM 88002

Director  
Defense Advanced Research Projects Agency  
ATTN: LTC C. Buck  
1400 Wilson Boulevard  
Arlington, VA 22209

Commander  
U.S. Army Materiel Command  
ATTN: AMCDRA-ST  
5001 Eisenhower Avenue  
Alexandria, VA 22304

NASA  
Langley Research Center  
ATTN: MS 168, G. B. Northham  
Hampton, VA 23365

Commander  
U.S. Army Watervliet Arsenal  
ATTN: SARWV-RD, R. Thierry  
Watervliet, NY 12189

Director  
U.S. Army Air Mobility Research  
and Development Laboratory  
Ames Research Center  
Moffett Field, CA 94035

Commander  
U.S. Army Electronics Research  
and Development Command  
ATTN: AMSEL-ED  
DELSD-L  
Fort Monmouth, NJ 07703-5301

Commander  
U.S. Army Missile Command  
ATTN: AMSMI-R  
AMSMI-YDL  
AMSMI-RK, D. J. Ifshin  
W. Wharton  
Redstone Arsenal, AL 35809-5252

Commander  
U.S. Army Natick Research  
and Development Command  
ATTN: AMXRE, D. Sieling  
Natick, MA 01762

Commander  
U.S. Army Tank Automotive Research  
and Development Command  
ATTN: AMSTA-TSL  
Warren, MI 48090

Commander  
U.S. Army White Sands Missile Range  
ATTN: STEWS-VT  
White Sands Missile Range, NM 88002

Commander  
U.S. Army Materials and  
Mechanics Research Center  
ATTN: AMXMR-ATL  
Watertown, MA 02172

Commander  
U.S. Army Research Office  
ATTN: Technical Library  
D. Squire  
F. Schmiedeshaff  
R. Ghirardelli  
M. Ciftan  
P.O. Box 12211  
Research Triangle Park, NC 27706-2211

Office of Naval Research  
ATTN: Code 473  
G. Neece  
Code 432, R. S. Miller,  
800 N. Quincy Street  
Arlington, VA 22217

Commander  
Naval Sea Systems Command  
ATTN: J. W. Murrin, SEA-62R2  
National Center  
Bldg 2, Room 6E08  
Washington, DC 20362

Commander  
Naval Surface Weapons Center  
ATTN: Library Branch, DX-21  
G-23, J. L. East, Jr.  
Dahlgren, VA 22448

Commander  
Naval Surface Weapons Center  
ATTN: Code 240, S. J. Jacobs  
J. Sharma  
Code 730  
R-13, R. Bernecker  
R-16, G. B. Wilmot  
White Oak  
Silver Spring, MD 20910

Commander  
Naval Underwater Systems Center  
Energy Conversion Department  
ATTN: Code 5B331, R. S. Lazar  
Newport, RI 02840

Commander  
Naval Weapons Center  
ATTN: Code 389, R. Derr  
C. Thelen  
Code 3891, T. Boggs  
K. J. Graham  
China Lake, CA 93555

Commander  
Naval Research Laboratory  
ATTN: Code 6180, L. Harvey  
          J. McDonald  
          E. Oran  
          J. Shrur  
          Code 6110, R. J. Doyle  
Washington, DC 20375

Superintendent  
Naval Postgraduate School  
ATTN: Technical Library  
          Department of Aeronautics, D. Netzer  
Monterey, CA 93940

Commander  
Naval Ordnance Station  
ATTN: Charles Dale  
          Technical Library  
Indian Head, MD 20640-5000

Air Force Armament Laboratory  
ATTN: AFATL-DLODL  
Eglin Air Force Base, FL 32542-5000

AFOSR  
ATTN: J. F. Masi  
          B. T. Wolfson  
          J. M. Tishkoff  
          D. Ball  
          L. Caveny  
Bolling Air Force Base  
Washington, DC 20332

AFRPL (DRSC)  
ATTN: D. George  
          R. Geisler  
          B. Goshgorian  
          W. Roe  
          D. Weaver  
          J. N. Levine  
Edwards AFB, CA 93523-5000

National Bureau of Standards  
U.S. Department of Commerce  
ATTN: J. Hastie  
          T. Kashiwagi  
          H. Semerjian  
          M. Jacox  
          S. Ray  
          A. Carasso  
          K. Smyth

G. Rossasco  
J. Stevenson  
Washington, DC 20234

Lockheed Palo Alto Research Laboratories  
ATTN: Technical Information Center  
Dept 52-35, George Lo  
3521 Hanover Street  
Palo Alto, CA 94304

Aerojet Solid Propulsion Co.  
ATTN: P. Micheli  
Sacramento, CA 95813

Atlantic Research Corporation  
ATTN: M. K. King  
5390 Cherokee Avenue  
Alexandria, VA 22314

Atlantic Research Corporation  
ATTN: R.H.W. Waesche  
7511 Wellington Road  
Gainsville, VA 22065

AVCO Corporation  
AVCO Everett Research Laboratory  
Division  
ATTN: D. Stickler  
2385 Revere Beach Parkway  
Everett, MA 02149

Calspan Corporation  
ATTN: E. B. Fisher  
A. P. Trippe  
P.O. Box 400  
Buffalo, NY 14221

General Electric Armament  
and Electrical Systems  
ATTN: M. J. Bulman  
Lakeside Avenue  
Burlington, VT 05401

General Electric Company  
Flight Propulsion Division  
ATTN: Technical Library  
Cincinnati, OH 45215

Hercules Powder Company  
Alleghany Ballistic Lab  
ATTN: R. Miller  
Technical Library  
Cumberland, MD 21501

Hercules, Incorporated  
Bacchus Works  
ATTN: B. Isom  
K. P. McCarty  
P.O. Box 98  
Magna, UT 84044

IITRI  
ATTN: M. J. Klein  
10 West 35th Street  
Chicago, IL 60615

Olin Corporation  
Badger Army Ammunition Plant  
ATTN: J. Ramnarace  
Baraboo, WI 53913

Applied Combustion Technology, Inc.  
ATTN: A.M. Varney  
P.O. Box 17885  
Orlando, FL 32860

Olin Corporation  
New Haven Plant  
ATTN: R. L. Cook  
D. W. Riefler  
275 Winchester Avenue  
New Haven, CT 06504

Paul Gough Associates, Inc.  
ATTN: P. S. Gough  
P.O. Box 1614  
Portsmouth, NH 03801

Physics International Company  
2700 Merced Street  
Leandro, CA 94577

Rockwell International Corp.  
Rocketdyne Division  
ATTN: C. Obert  
J. E. Flanagan  
A. Axeworthy  
6633 Canoga Avenue  
Canoga Park, CA 91304

Rockwell International Corp.  
Rocketdyne Division  
ATTN: W. Haymes  
Technical Library  
McGregor, TX 76657

Science Applications, Inc.  
ATTN: R. B. Edelman  
23146 Cumorah Crest  
Woodland Hills, CA 91364

Thiokol Corporation  
Elkton Division  
ATTN: E. Sutton  
W. N. Brundige  
Elkton, MD 21921

Thiokol Corporation  
Huntsville Division  
ATTN: D. Flanigan  
R. Glick  
Technical Library  
Huntsville, AL 35807

Thiokol Corporation  
Wasatch Division  
ATTN: J. Peterson  
Technical Library  
P.O. Box 524  
Brigham City, UT 84302

BDM Corporation  
ATTN: T. P. Goddard  
2600 Cearden Road  
North Building  
Monterey, CA 93940

TRW Systems Group  
ATTN: H. Korman  
One Space Park  
Redondo Beach, CA 90278

United Technologies  
Chemical Systems Division  
ATTN: R. Brown  
Technical Library  
P.O. Box 358  
Sunnyvale, CA 94086

Battelle Memorial Institute  
ATTN: Technical Library  
R. Bartlett  
505 King Avenue  
Columbus, OH 43201

Brigham Young University  
Department of Chemical Engineering  
ATTN: M. W. Beckstead  
Provo, UT 84601

California Institute of Technology  
204 Karmar Lab  
Mail Stop 301-46  
ATTN: F. E. C. Culick  
1201 E. California Street  
Pasadena, CA 91125

Georgia Institute of Technology  
School of Aerospace Engineering  
ATTN: B. T. Zinn  
E. Price  
W. C. Strahle  
Atlanta, GA 30332

Institute of Gas Technology  
ATTN: D. Gidaspow  
3424 S. State Street  
Chicago, IL 60616

Johns Hopkins University/APL  
Chemical Propulsion Information Agency  
ATTN: T. Christian  
Johns Hopkins Road  
Laurel, MD 20810

Massachusetts Institute of Technology  
Department of Mechanical Engineering  
ATTN: T. Toong  
Cambridge, MA 02139

Massachusetts Institute of Technology  
Laboratory for Information and Decision Systems  
ATTN: A. S. Willsky  
Cambridge, MA 02139

Pennsylvania State University  
Applied Research Laboratory  
ATTN: G. M. Faeth  
P.O. Box 30  
State College, PA 16801

Pennsylvania State University  
Department of Mechanical Engineering  
ATTN: K. Kuo  
University Park, PA 16801

Pennsylvania State University  
Department of Material Sciences  
ATTN: H. Palmer  
University Park, PA 16801

Princeton Combustion Research Laboratories  
ATTN: M. Summerfield  
N. Messina  
475 U.S. Highway One North  
Monmouth Junction, NJ 08852

Princeton University  
Forrestal Campus  
ATTN: I. Glassman  
K. Brezinsky  
F. Dryer  
Technical Library  
P.O. Box 710  
Princeton, NJ 08540

Princeton University  
MAE Department  
ATTN: F. A. Williams  
Princeton, NJ 08544

Polytechnic Institute of NY  
ATTN: S. Lederman  
Route 110  
Farmingdale, NY 11735

Purdue University  
School of Mechanical Engineering  
ATTN: J. Osborn  
S. N. B. Murthy  
N. M. Laurendeau  
TSPC Chaffee Hall  
West Lafayette, IN 47906

Purdue University  
School of Aeronautics and Astronautics  
ATTN: R. Glick  
West Lafayette, IN 47906

Rutgers State University  
Department of Mechanical and Aerospace Engineering  
ATTN: S. Temkin  
University Heights Campus  
New Brunswick, NJ 08903

SRI International  
ATTN: Technical Library  
D. Crosley  
J. Barker  
D. Golden  
G. Smith  
333 Ravenswood Avenue  
Menlo Park, CA 94025

Stevens Institute of Technology  
Davidson Laboratory  
ATTN: R. McAlevy  
Hoboken, NJ 07030

United Technology  
ATTN: Alan Ecbreth  
Robert Hall  
Gregory Dobbs  
Research Center  
East Hartford, CT 06108

General Motors Corporation  
ATTN: J. H. Bechtel  
R. Teets  
Warren, Michigan 48090

System Research Laboratory  
ATTN: L. Goss  
2600 Indian Ripple Rd  
Dayton, Ohio 45440

University of California  
Lawrence Livermore National Laboratory  
ATTN: Library  
A. C. Buckingham  
Livermore, CA 94550

Exxon Research and Engineering Company  
ATTN: A. Dean  
M. Chou  
P.O. Box 8  
Linden, NJ 07036

Ford Motor Company  
Research Staff  
ATTN: K. Marko  
L. Rimal  
Dearborn, Michigan 48120

Sandia National Laboratories  
Combustion Sciences Department  
ATTN: R. Cattolua  
D. Stephenson  
P. Mattern  
Livermore, CA 94550

Sandia National Laboratories  
ATTN: M. Smoke  
Division 8353  
Livermore, CA 94550

Rensselaer Polytechnic Institute  
Dept. of Chem. Engineering  
ATTN: A. Fontijn  
Troy, NY 12181

University of California, San Diego  
AMES Department  
ATTN: F. Williams  
La Jolla, CA 92037

University of California, San Diego  
Energy Center and Department  
of Applied Mechanics  
ATTN: S. S. Penner  
La Jolla, CA 92037

University of California  
Dept. of Mechanical Engr  
ATTN: J. W. Daily  
Berkeley, CA 94720

University of Dayton Research Inst  
ATTN: D. Campbell  
Dayton, OH 45406

University of Florida  
Dept. of Chemistry  
ATTN: J. Winefordner  
Gainesville, Florida 32601

University of Illinois  
Dept. of Mechanical Eng.  
ATTN: H. Krier  
S. L. Soo  
144 MEB, 1206 W. Green St.  
Urbana, IL 61801

University of Minnesota  
Dept. of Mechanical Engr  
ATTN: E. Fletcher  
Minneapolis, MN 55455

University of California,  
Santa Barbara  
Quantum Institute  
ATTN: K. Schofield  
M. Steinberg  
Santa Barbara, CA 93106

University of Southern California  
Department of Chemistry  
ATTN: S. Benson  
Los Angeles, CA 90007

Stanford University  
Department of Mech Eng  
ATTN: R. Hanson  
Stanford, CA 93106

Stanford University  
Department of Physics  
ATTN: A. Macovski  
Palo Alto, CA 94305

University of Texas  
Department of Chemistry  
ATTN: W. Gardiner  
H. Schaefer  
Austin, TX 78712

University of Utah  
Dept. of Chemical Engineering  
ATTN: A. Baer  
G. Flandro  
Salt Lake City, UT 84112

END

FILMED

3 - 86

DTIC